A network of coiled-coil and actin-like proteins controls the cellular organization of magnetosome organelles in deep-branching magnetotactic bacteria

Virginia V. Russell[1], Anthony T. Iavarone[2], Ertan Ozyamak[1,3], Carly Grant[1,4] and Arash Komeili[1]

[1] Plant and Microbiology, University of California Berkeley, Berkeley, California, USA.
[2] QB3/Chemistry Mass Spectrometry Facility, University of California Berkeley, Berkeley, California, USA.
[3] Current affiliation: Bio-Rad Laboratories, Hercules, California, USA
[4] Current affiliation: Entrepreneurship Program, UCSF Rosenman Institute, San Francisco, California, USA

Abstract

Magnetotactic Bacteria (MTB) are a diverse group of microorganisms that use magnetosomes, organelles composed of magnetite or greigite, to navigate along geomagnetic fields. While MTB span several phyla and exhibit diverse phenotypes, magnetosome formation has been mechanistically studied in only two species of *Alphaproteobacteria*. Here, we use *Desulfovibrio magneticus* RS-1 to uncover the mechanisms behind tooth-shaped magnetosome assembly in deep-branching MTB. Our findings reveal that RS-1 magnetic particles initially form randomly within the cell before localizing to the positive cell curvature. Genetic and proteomic analyses indicate that early biomineralization involves membrane-associated proteins found in all MTB, while later stages depend on coiled-coil (Mad20, 23, 25, and 26) and actin-like (MamK and Mad28) proteins, most of which are unique to deep-branching MTB. These findings suggest that while biomineralization originates from a common ancestor, magnetosome chain formation has diverged evolutionarily among different MTB lineages.

Introduction

Magnetotactic Bacteria (MTB) are a diverse group of microorganisms that navigate along geomagnetic fields to locate low-oxygen environments in a process termed magneto-aerotaxis. This ability relies on magnetosomes—specialized organelles containing magnetic crystals of magnetite (Fe_3O_4) or greigite (Fe_3S_4) 50-70 nm in diameter, enclosed by a lipid bilayer membrane with unique set of proteins[1,2]. Depending on the species, magnetosomes form single or multiple chains, that allow for alignment with external fields[3]. These features have made MTB models for studying bacterial organelle formation, biomineralization, and the global

35 geochemical cycling of iron[4]. MTB have also been deployed as potential vehicles for a variety of
36 biotechnological applications[5]. A key bottleneck in the study of MTB has been the limited
37 number of model organisms that sufficiently represent the mechanistic diversity and evolution of
38 magnetosome formation.

39 MTB are a polyphyletic group of microorganisms that belong to *Alphaproteobacteria*,
40 *Gammaproteobacteria*, *Candidatus Etaproteobacteria* classes in the *Pseudomonadota* phylum,
41 and the phyla *Desulfobacterota*, *Nitrospirota, Candidatus Omnitrophota*, and *Elusimicrobiota*
42 (Figure 1B). Metagenomic studies suggest MTB may also exist in the *Latescibacteria*,
43 *Planctomycetes*, *Nitrospinota*, *Fibrobacterota*, *Riflebacteria*, *Hydrpgendentota*, *Myxococcota*,
44 *Bdellovibrionota* phyla and possibly more[2,6]. MTB exhibit diverse phenotypes, including
45 variations in crystal shape, chain organization, and magnetosome composition[3]. Phylogeny
46 correlates with some of these features; for instance, *Alphaproteobacteria* produce
47 cubooctahedral and prismatic magnetite crystals, while *Desulfobacterota* and other deep-
48 branching MTB (*Nitrospirota*, *Omnitrophota*, *Elusimicrobiota*) form irregular tooth-shaped
49 magnetite crystals thought to represent the ancestral magnetosome form[3](Figure 1C).

50 Despite the vast diversity of MTB, most mechanistic studies have focused on two
51 Alphaproteobacterial species, *Magnetospirillum magneticum* AMB-1 and *Magnetospirillum*
52 *gryphiswaldense* MSR-1, which contain a conserved magnetosome gene cluster (MGC). The
53 MGC spans ~100 kilobases and includes 50-100 genes, with 29 necessary and sufficient for
54 magnetosome formation[7]. Among these, only five core genes (*mamA*, *B*, *I*, *E*, and *Q*) are shared
55 across all MTB[8,9]. Many genes critical for magnetosome formation in *Alphaproteobacteria* are
56 absent in other MTB. Other sets of conserved genes, called *mad* (**ma**gnetosome **d**eep
57 branching) are found in all deep-branching MTB, *man* (**ma**gnetosome **n**itrospirota) genes are
58 found in *Nitrospirota*, and *mae* (**ma**gnetosome **e**lusimicrobiota) genes are found in
59 *Elusimicrobiota*[8]. However, few non-*Alphaproteobacterial* MTB are cultured, and most lack
60 genetic systems, limiting insights into *mad* gene function and irregular tooth-shaped
61 magnetosome formation. This is a critical barrier in the study of MTB as tooth-shaped
62 magnetosomes are common in nature[3], yet their biomineralization mechanisms remain
63 unknown.

64 The most promising model for deep-branching MTB is *Desulfovibrio magneticus* RS-1, a
65 sulfate-reducing obligate anaerobe from the *Desulfobacterota* phylum[10,11]. RS-1 synthesizes a
66 single chain of irregular tooth-shaped magnetite magnetosomes, organized into subchains of
67 contiguous crystals separated by gaps along the positive cell curvature (Supplemental Figure
68 S4E, Figure 2D-*ii*). It is one of the few cultured non-Alphaproteobacterial MTB with a sequenced

genome and the only deep-branching strain with tools for heterologous gene expression and genome editing[12–14]. Previous studies of RS-1 have highlighted several features distinguishing it from *Alphaproteobacterial* models. First, RS-1 produces tooth-shaped crystals. Second, unlike *Alphaproteobacteria*, mature RS-1 crystals appear to lack a lipid membrane[15], though its MGC contains transmembrane domain proteins. Genetic studies show mutations in these genes disrupt magnetite formation, implying the involvement of a magnetosome membrane at some stage[12]. Finally, RS-1, like all deep-branching MTB, contains a suite of *mad* genes, most of which do not have known functions.

Here, we comprehensively characterize the RS-1 biomineralization process using proteomics and genetics to define new pathways of magnetosome formation unique to deep-branching MTB. Using a conditional biomineralization assay combined with genetics and proteomics, we define specific steps in magnetic particle growth and identify specific factors associated with the progression of biomineralization and magnetosome chain formation. We find that early steps of biomineralization utilize proteins enriched in transmembrane domains including some encoded by *mam* genes common to all MTB. In contrast, localization, organization and positioning of the magnetosome chain rely on a suite of coiled-coil domain-containing Mad proteins as well as the actin-like proteins, MamK and Mad28. These findings indicate a complex evolutionary history where iron biomineralization is ancestral feature of all MTB while chain formation follows a divergent group-specific path.

Results

Hydrogen inhibition of magnetosome synthesis

Our first goal was to develop a robust system to visualize the steps of magnetosome formation in RS-1. In other MTB, magnetite is not formed under iron-limiting conditions. Addition of iron then triggers synchronized magnetosome chain development[16]. However, transitioning from iron-limited to iron-replete conditions in RS-1 leads to the accumulation of ferrosomes[15] — organelles involved in storage and detoxification of iron[17,18]. The abundance and appearance of ferrosomes in electron microscopy obscure magnetosomes, making it impossible to visualize the early stages of magnetite biomineralization. To overcome this limitation, we sought an alternative method of magnetosome inhibition that avoids iron starvation.

Serendipitously, we discovered that growth in hydrogen instead of nitrogen headspace significantly reduces RS-1's magnetic response (measured as the coefficient of magnetism (C_{Mag})[19]) (Figure 2A). A trace magnetic response at high hydrogen concentrations suggested the

need for hydrogen exposure throughout the culture medium. To test this, we flushed both the headspace and medium with 5% hydrogen and grew cells while spinning. Under these conditions, cultures showed no magnetic response as indicated by a C_{Mag} of 1 (Figure 2C), and absence of magnetosomes when viewed by transmission electron microscopy (TEM) (Figure 2D).

One explanation for these observations is that hydrogen inhibits RS-1 growth, indirectly preventing magnetosome formation. However, growth measurements showed similar final cell densities in hydrogen and nitrogen (Figure 2B), with hydrogen-grown cells doubling faster (6 vs. 8 hours) (Figure 2B). Another possibility is that hydrogen limits iron uptake, restricting magnetosome production. To test this, we used the post-iron-starvation accumulation of ferrosomes as a proxy for iron uptake. Cells were grown in hydrogen and iron-limiting conditions and subsequently exposed to iron with either a nitrogen or hydrogen headspace. Ferrosomes were formed in both nitrogen and hydrogen (Figure 2E *iii* and *iv*), but magnetosomes formed only in nitrogen conditions (Figure 2E-*iv*). This indicates hydrogen does not inhibit iron uptake. Finally, abundance of magnetosome proteins does not change significantly at a global level (Extended Results).

Characteristics of early and late stages of biomineralization

We next hypothesized that switching from hydrogen to nitrogen conditions under iron replete conditions could restore magnetosome formation without ferrosome interference. To test this, RS-1 was grown with 10% hydrogen to eliminate magnetosomes, then transferred to nitrogen infused medium. As predicted, magnetic response increased over time (Figure 2F), no ferrosomes were formed, and only magnetosomes were observed (Figure 2G *i-iii*). This transition provides a reliable method to synchronize magnetosome formation and study biomineralization.

To capture early stages of biomineralization, RS-1 was incubated shaking in hydrogen-infused medium for several passages to eliminate existing magnetosomes (Figure 2D-*i*). Cells were then transferred to nitrogen-infused medium and harvested once a measurable magnetic response (C_{Mag} 1.05-1.15) was detected. Early timepoints in biomineralization showed an average of 3 magnetosomes per cell (Figure 3A, 3C). Many cells contained both mature and immature crystals (Figure 3A-*ii*). The median crystal length was 38 nm, with a bimodal distribution indicating both immature and mature crystals present (Figure 3D). Similarly, the shape factor (width-to-length ratio) followed a bimodal pattern, with peaks around 1 for immature and 2 for mature crystals (Figure 3E). During the late stages of biomineralization (C_{Mag}

137 1.3-1.5), cells contained complete magnetosome chains composed of smaller subchains (Figure
138 3B), averaging 12 crystals per cell (Figure 3C), all localized to the positive cell curvature. The
139 average crystal length was 51 nm with a shape factor of 1.7, both fitting a normal distribution
140 due to presence of fewer immature crystals (Figure 3D, 3E). These findings point to a crystal
141 growth pattern similar to that proposed for other deep-branching MTB[20]. RS-1 crystals nucleate
142 and grow equidimensionally to approximately 30 nm before elongating anisotropically at one
143 end to produce a tooth-shaped morphology (Figure 3G). High-magnification TEM images
144 revealed two mature magnetosome morphologies: curved and straight (Figure 3F *ix* and *x*).
145 Perhaps, during elongation, crystals develop into either a straight or curved form (Figure 3F-*v*,
146 3F-*vi*).
147 While observing biomineralization stages, we discovered that subcellular magnetosome
148 location correlates with crystal maturation. In early stages, nearly all mature crystals are
149 positioned at the positive cell curvature, where magnetosome chains typically form, but only
150 about 25% of immature crystals are located there (Figure 3H, 3I). In contrast,
151 *Alphaproteobacterial* MTB such as AMB-1 and MSR-1, localize magnetosome membranes to
152 the positive curvature before biomineralization begins[2,21].
153
154 **Distinct proteomes differentiate early- and late-stage magnetosomes**
155 We next investigated if specific cohorts of proteins were associated with distinct
156 biomineralization stages. Cells from early and late stages were harvested and lysed, and
157 magnetosomes were isolated using a magnetic column. Proteomic analysis of cell lysates and
158 magnetosome fractions via liquid chromatography-mass spectrometry focused on RS-1 MGC-
159 encoded proteins enriched at each stage. Early-stage magnetosomes were enriched for Mad10,
160 MamB, MamA, Mad4, FmpA, FmpB, and MamEO-Cter (Figure 3J), many of which contain
161 predicted transmembrane domains. Late-stage magnetosomes were enriched for Mad20,
162 Mad23, Mad28, and MamK, all of which lack transmembrane domains (Supplemental Figure
163 3A). The actin-like domains in Mad28 and MamK (Supplemental Figure 3A) suggest roles in
164 chain alignment and organization. These results reveal a shift in membrane association and
165 chain organization from early to late stages.
166
167 **Early magnetosome proteins regulate biomineralization activity**
168 We next turned to genetics to provide functional evidence for stage-specific action of
169 magnetosome proteins. Previous studies using chemical and UV mutagenesis identified RS-1
170 mutants with severe biomineralization defects, including several alleles of *mamB* that lack a

171 magnetic response and do not produce crystals[12]. This phenotype corroborates our finding that
172 MamB preferentially associates with early-stage magnetosomes (Figure 3J).
173 In contrast to *mamB*, mutants in *fmpA* and *fmpB* can still produce some magnetic
174 particles[12]. Both FmpA and FmpB contain transmembrane domains and serine
175 protease/denitrogenase Fe-Mo domains and are enriched on magnetosomes at the early stages
176 of biomineralization (Supplemental Figure 3A and Figure 3J). Detailed TEM analysis revealed
177 distinct defects for each strain: *fmpA* mutants produce misshaped circular or symmetrical
178 crystals (Figure 4A, G), while *fmpB* mutants form smaller WT-like crystals, some of which are
179 misshaped (Figure 4B, H). Consistent with previous findings[12], both mutants exhibit significantly
180 fewer crystals per cell, smaller crystal sizes, and a reduced shape factors as compared to WT
181 (Figure 4D, 4E, and 4F).
182 In addition to the defects in crystal shape and size, *fmpA* and *fmpB* mutants exhibited
183 abnormal crystal placement with most crystals not localized to the cell's positive curvature
184 (Figure 4J). The crystals of the *fmpA* mutant also fail to form chains, while only 5% of *fmpB*
185 mutant cells show chain organization (Figure 4I). These findings suggest FmpA and FmpB are
186 crucial for early magnetosome synthesis and indicate that biomineralization likely initiates away
187 from the positive curvature. We propose that crystal nucleation occurs throughout the cell and
188 crystals are later transported to the positive curvature post-maturation. Without FmpA and
189 FmpB, crystals could remain "stuck" at nucleation sites, blocking their relocation and preventing
190 new crystal formation, resulting in fewer crystals in mutant cells (Figure 4D).
191
192 **Initiation of chain formation by Mad10**
193 Mad10 is more abundant in early-stage magnetosome samples than in late stages and
194 has the highest abundance ratio among MGC proteins at the magnetosome compared to the
195 cell lysate under all conditions (Supplemental Figure 8A). Previous studies identified Mad10 as
196 a magnetite-binding protein[22,23] and hypothesized a role in magnetite nucleation or shape
197 control. To investigate its function, we deleted *mad10* in RS-1 via allelic exchange. The Δ*mad10*
198 mutant shows a significantly reduced magnetic response, which is restored by plasmid-based
199 *mad10* expression (Supplemental Figure 1B, 1C). Despite the low Cmag, however, crystal size
200 and shape remain unchanged and, instead, magnetosomes cluster in a single location within
201 the cell (Figure 5A, Supplemental Figure 1I). Crystal numbers also vary widely per cell
202 (Supplemental Figure 1D), likely due to unequal distribution during cell division. These findings
203 indicate that Mad10 is essential for magnetosome chain organization but not for crystal size or
204 shape regulation (Figure 5A).

205

206 **A module of Mad proteins assembles the magnetosome subchain**

207 We next targeted genes encoding proteins more abundant in late stages of
208 biomineralization (Figure 3J) and neighboring genes potentially belonging to the same operon
209 (Figure 1A). All deletions were successfully complemented via plasmid-based expression
210 (Supplemental Figures 1C, 6A-G). Mutants exhibited a range of defects which were quantified
211 based on chain placement, magnetosome distribution, and chain/subchain phenotypes
212 (Supplemental Figure 7F-I).

213 This analysis identified Mad20, Mad23, Mad25, and Mad26 as a module for
214 magnetosome subchain assembly in RS-1. In the Δ*mad23* mutant, single magnetosomes are
215 dispersed, with the fewest crystals per subchain among mutants and WT (Figure 5C,
216 Supplemental Figure 1E, 6J). The strain also has the lowest C_{Mag} of all chain organization
217 mutants (Supplemental Figure 1B), suggesting Mad23 connects individual magnetosomes to
218 form subchains. In contrast, the Δ*mad20* mutant forms distinct subchains, some linear, and
219 others in the form of rings, clusters, or curved lines (Figure 5B). It has fewer subchains than WT
220 (Supplemental Figure 1F, 6I), but each contains more magnetosomes (Supplemental Figure
221 1E). This suggests Mad20 regulates crystal influx into subchains; without it, excess crystals
222 cause curling and distortion (Supplemental Figure 6I). Δ*mad25* and Δ*mad26* mutants show
223 similar phenotypes (Figure 5D-E), with subchain and crystal numbers comparable to WT
224 (Supplemental Figure 1F, D). However, most subchains cluster or form rings, especially in
225 Δ*mad26*, where ~80% cluster and 15% form rings (Supplemental Figure 7E). These findings
226 indicate Mad25 and Mad26 are essential for maintaining subchain linearity.

227 Overall, these mutants reveal an RS-1 magnetosome chain organization distinct from
228 *Alphaproteobacterial* MTB. In AMB-1, for example, TEM shows subchains of magnetic particles,
229 separated by empty magnetosome membranes all of which are organized into a continuous
230 chain[24]. In contrast to AMB-1, some RS-1 mutants exhibit clusters, rings, or curved subchains
231 within the same cell, suggesting subchains are a fundamental structural unit of chain
232 architecture in RS-1.

233

234 **MamK and Mad28 control subchain separation and chain localization**

235 Mad28 and MamK were selected for genetic analysis due to their higher abundance in
236 late-stage magnetosomes (Figure 3J) and their actin-like domains (Supplemental Figures S3A
237 and S5). *mamK* is present in nearly all MTB and is well-studied in AMB-1 and MSR-1[21,25,26]. In
238 AMB-1, *mamK* deletion disrupts chain cohesion[21], creating gaps that affect equal distribution

239 during cell division[27]. In MSR-1, *mamK* deletion results in mislocalized chains, mostly away from
240 the mid-cell[28]. Similarly, in RS-1, we find that MamK plays a role in chain organization. Deletion
241 of *mamK* eliminated the subchain phenotype (Figure 5G, Supplemental Figure 1F), leading to a
242 single continuous chain, which sometimes wrapped around itself, resembling multiple chains.
243 These mutants also had more crystals per cell compared to WT (Figure 5N, Supplemental
244 Figure 1D).
245 RS-1, contains another magnetosome gene with an actin-like domain,
246 *mad28*[9,29](Supplemental Figure 3A), found in all deep-branching MTB and previously suggested
247 to have a similar role to MamK [29]. Surprisingly, deleting *mad28* in RS-1 resulted in a phenotype
248 distinct from that of the Δ*mamK*. In Δ*mad28*, WT-like subchain organization was retained.
249 However, chains were no longer exclusively localized to the positive cell curvature and were
250 found pole-to-pole at mid-cell, as well as organized diagonally or transversely across the cell
251 (Figure 5F, 5J, 5K).
252 To further distinguish between the Δ*mad28* and Δ*mamK* strains, we examined chain
253 formation in a biomineralization time-course experiment. In Δ*mad28*, chain assembly followed
254 the WT pattern, with a single mature crystal forming first, followed by subchain development and
255 crystal incorporation (Figure 5I-K). However, chains were mispositioned from the start, forming
256 pole-to-pole or diagonal/transverse orientations instead of localizing to the positive curvature as
257 in WT (Figure 5J-K). In contrast, Δ*mamK* exhibited a distinct chain formation pattern. Early
258 biomineralization resembled WT, but as crystals matured, subchains failed to develop, resulting
259 in a single continuous chain (Figure 5L). Δ*mamK* mutants also had more magnetosomes per
260 cell and a higher C_{Mag} than WT at both biomineralization stages (Figure 5N, 5M, Supplemental
261 Figure 1B), a phenotype not observed in other *mamK* mutants[21,28]. These findings suggest that
262 Mad28 aligns magnetosomes to the positive curvature early in chain formation, while MamK
263 distributes subchains along the cell length, ensuring proper alignment and potentially regulating
264 magnetosome production.
265
266 **Interaction Network of chain organization proteins**
267 Bioinformatic analysis shows that Mad10, 20, 23, 25, and 26 contain coiled-coil domains
268 which can facilitate a variety of protein-protein interactions[30] (Supplemental Figure 3A). Mad23
269 also has HEAT repeat domains, known for similar functions. Additionally, MamK and Mad28 can
270 form homo- and heteropolymers[29]. Thus, we hypothesized that these chain formation proteins
271 may interact with one another. To explore potential interactions, we conducted Bacterial
272 Adenylate Cyclase Two-Hybrid (BACTH) assays[31] (Supplemental Figure 2). We created N- and

273 C-terminal fusions to T25 and T18 domains for each protein and tested all interaction
274 combinations (Supplemental Figure 9). Interactions were classified based on color intensity:
275 dark blue spots as strong (+++), medium blue as moderate (++), and light blue as minor (+)
276 (Supplemental Figure 2B). Our results reveal an extensive and complex network of potential
277 interactions. All proteins exhibited self-interactions in at least one fusion combination. Mad25
278 interacted with all tested proteins, while Mad20, 23, 26, and MamK interacted with three or
279 more. Mad10, interacted with itself, Mad23, and Mad25. Mad28 interacted only with Mad25
280 (Supplemental Figure 2A-D). These findings provide further evidence for the existence of a
281 distinct chain organization pathway in deep-branching MTB, dependent on the interactions of
282 coiled-coil and actin-like proteins.
283
284 **Discussion**
285 In this study, we used a new workflow to track biomineralization in *Desulfovibrio*
286 *magneticus* RS-1, a representative of deep-branching MTB, to describe an organelle assembly
287 process distinct from *Alphaproteobacterial* species. Our work suggests a new model of
288 magnetosomes formation with the following steps (Figure 6):
289 **Step 1: Nucleation and Growth.** Biomineralization initiates at randomly distributed membrane-
290 bounded nucleation sites that are likely membrane-enclosed. Mutations in *fmpA* and *fmpB*
291 impair crystal maturation, reduce crystal numbers, and disrupt localization to the positive
292 curvature, linking biomineralization to chain formation. **Step 2: Crystal Maturation and**
293 **Localization.** As crystals mature, they are transported to the cell's positive curvature. Based on
294 findings here and in previous work, we suggest that at some stage during biomineralization
295 magnetite crystals are released from the membrane. Mad10, previously shown to interact with
296 magnetite[22], may facilitate this transition. Bacterial two-hybrid results suggest an assembly
297 pathway where Mad10 interacts with Mad23, which subsequently connects to Mad25. **Step 3:**
298 **Subchain Assembly.** Initially, one or two mature crystals appear at the positive curvature.
299 Mad23 links accumulating crystals to form subchains, which may be stabilized by Mad25 and
300 Mad26. **Step 4: Chain Elongation and Positioning.** In parallel to the previous steps,
301 subchains are distributed along the cell length by MamK, while Mad28 ensures their localization
302 to the positive curvature. MamK's role in chain organization is conserved across MTB, as RS-1
303 MamK can partly complement *mamK* loss in MSR-1[29]. However, RS-1 MamK has unique
304 functions, as its absence results in the loss of subchains and the formation of longer chains with
305 more crystals per cell. Interestingly, Mad28 from deep-branching MTB partially complements

306 MamK loss in MSR-1[29], but our findings suggest Mad28 primarily localizes the chain, while
307 MamK organizes it.
308 This model reveals several key differences between RS-1 and other established model
309 organisms. First, biomineralization in RS-1 occurs one or a few crystals at a time and is a
310 prerequisite step for chain formation, whereas in Alphaproteobacterial MTB, magnetosome
311 membranes form chains independently of biomineralization[32]. Second, RS-1 magnetosomes
312 have a dynamic proteome that changes with biomineralization stages, while, with a few
313 exceptions, AMB-1 and MSR-1 maintain a largely constant proteome[2,33,34]. Finally, RS-1 and
314 Alphaproteobacterial MTB use different sets of proteins for chain formation. The domain
315 architecture of their respective magnetosome proteins provide further evidence for the unique
316 features of each MTB group. For instance, 67% of AMB-1 magnetosome proteins, but only 38%
317 RS-1's, are predicted to contain transmembrane domains (Supplemental Figure 4A-B).
318 However, nearly ~24% (10 proteins) of RS-1 magnetosome proteins contain predicted coiled-
319 coil domains, in contrast to ~6% (3 proteins) of AMB-1's magnetosome proteins (Supplemental
320 Figure 4C-D). Additionally, other than MamK, all known magnetosome chain formation factors of
321 AMB-1 and MSR-1 (MamJ, MamY, LimJ, MamK-like, McaA, and McaB) are absent in RS-1.
322 Similarly, MTB of the deep-branching *Elusimicrobiota* phylum which do not form organized
323 magnetosome chains are missing MamK as well as the chain formation Mad proteins.
324 Therefore, we suggest that these coiled-coil proteins, which may organize into intermediate
325 filaments similar to other bacterial proteins, along with the actin-like MamK and Mad28,
326 represent a mode of chain organization unique to deep-branching MTB.
327 Collectively, our findings shed further light on the evolution and diversification of
328 magnetosomes. Nearly all MTB share genes involved in membrane formation (*mamQ*), iron
329 transport (*mamB*), and chain organization (*mamK*), likely forming the foundations of an ancient
330 iron-accumulating organelle. Diverse magnetosome phenotypes, such as crystal shape
331 variations, may have emerged through addition of subgroup-specific proteins to this core
332 system. In our model, RS-1 and other deep-branching MTB evolved to organize biominerals into
333 chains using Mad proteins, while Alphaproteobacterial MTB developed a system to align
334 magnetosome membranes into chains using Mam proteins. This evolutionarily distinct solution
335 may have arisen to combat the previously described conflict between magnetocrystalline
336 orientation of tooth-shaped magnetosomes and their function as a navigational tool[35,36].
337
338 **Methods**
339

340 **Multiple-sequence alignments and tree construction**

341 Dataset was designed by searching IMG/M ER[37] for all known MTB species with
342 homologs for all five of the core *mam* genes selected: *mamK*, *mamA*, *mamB*, *mamM* and
343 *mamQ.* Next, the dataset was refined to encompass only species with available genomes and
344 accessible TEM images, enabling the identification of magnetosome gene sets (*mam*, *mms*,
345 *mad*, *man* and *mae*) for each species, along with their respective crystal shapes and
346 compositions. Supplemental table 1 is a list of all species included in designing the phylogenetic
347 tree for this analysis. Once the dataset was complete, the 16S DNA sequences for each species
348 were obtained from NCBI or IMG-M [37] (Supplemental table 1). Sequences were aligned using
349 MAFFT version 7.490 using the scoring matrix 1PAM/ k=2 [38]. Next, the aligned sequences were
350 used to generate the maximum likelihood tree using PhyMLTree version 3.3.20180621 using
351 GTR substitution model with 1000 bootstraps [39]. Additionally, the tree was rooted with
352 *Omnitrophus magneticus* SKK-01.

353

354 **General Culturing for RS-1**

355 *Desulfovibrio magneticus* RS-1 strains were grown at 30°C anaerobically in RS-1 growth
356 medium (RGM), as described previously [12,15]. For growth with hydrogen, the medium was
357 gassed with 10% hydrogen balanced with Nitrogen prior to autoclaving the medium.
358 Additionally, after inoculating, the headspace was re-gassed with the same concentration of
359 hydrogen/nitrogen gas mixture for 10 minutes. All hydrogen cultures were grown spinning on a
360 wheel in the 30°C incubator. Cultures with nitrogen in the headspace that were used as controls
361 for these hydrogen cultures were grown on a wheel in the incubator. All other nitrogen cultures
362 were grown without shaking.

363 For experiments with different concentrations of hydrogen (Figure 2A), RS-1 WT strain
364 was grown at 30°C anaerobically in RS-1 growth medium (RGM), as described above. Initially,
365 all culture tubes were purged with nitrogen gas. Subsequently, prior to inoculation, varying
366 volumes of nitrogen from the headspace were displaced and substituted with an equivalent
367 volume of 100% hydrogen gas, aiming to achieve distinct concentrations of hydrogen in the
368 headspace. Afterwards, RS-1 was inoculated into the culture tubes. Optical density and
369 magnetic response via C_{mag} was monitored throughout growth as previously described [12].

370

371 **Culturing for proteomics**

372 Cultures for hydrogen vs. nitrogen consisted of 350 mL cultures with 2/3 volume of
373 headspace, which were prepared by gassing either with nitrogen or 10% hydrogen and grown

374 by shaking at room temperature. At late exponential phase, cultures were harvested by
375 centrifugation at 8,000 rpm using the Beckman Model J2-21M/E centrifuge. Cell pellets were
376 stored at -80°C until lysis and preparation for proteomic analysis. To examine different stages of
377 biomineralization, 300 mL initial cultures were grown with hydrogen in the headspace to remove
378 all magnetosomes. C_{mag} was measured as described previously[12] and TEM images were taken
379 of initial cultures to ensure no magnetosomes were present. Then 10 1L bottles of RGM-X
380 medium were prepared by infusing the medium with nitrogen and gassing the headspace with
381 nitrogen. Each of the 3 biological replicates consisted of 10 1L bottles, which were inoculated
382 with the same starting culture. Three bottles were used for late biomineralization, which were
383 inoculated with 10 mL of starting culture, and seven bottles were used for early
384 biomineralization samples, which were inoculated with 20 mL of the starting culture. The
385 cultures were grown in a 30°C incubator and OD and C_{mag} were taken 2X daily. When cultures
386 reached a C_{mag} of 1.05-1.15 seven of the bottles were harvested for early biomineralization
387 samples by centrifugation at 8,000 RPM. Subsequently, when the final 3 bottles had a C_{mag}
388 between 1.30-1.5 they were harvested for late stages of biomineralization samples also by
389 centrifugation at 8,000 RPM. Cell pellets were stored at -80°C until it was time to prepare
390 samples for proteomics. Each biological replicate originated from a single colony, which was
391 inoculated into 200 mL pre-culture bottles grown with hydrogen. Each 200 mL pre-culture was
392 subsequently used to inoculate a set of ten 1L bottles, resulting in three 10L cultures derived
393 from three separate colonies.
394
395 **Collecting proteins associated with magnetosomes using a magnetic column**
396 After harvesting cultures, cell pellets were resuspended in buffer A (25 mM Tris, pH 7.0,
397 100 mM sucrose, 1 µg/mL Leupeptin, 1 µg/mL Pepstatin A, and 1 mM PMSF. Cells were lysed
398 three times at 25 kpi using the Single Shot feature of the Multi Cycle (MC) Cell Disruptor from
399 Constant Systems[40]. Magnetic LS Columns (130-042-401) from Miltenyi Biotec were used to
400 separate the magnetosomes from the cell lysate. Magnetic columns were primed with a wash
401 with buffer A, followed by the attachment of magnets to the outside of the columns.
402 Subsequently, the cell lysate was passed through the column by gravity flow. Flow through
403 fractions were passed over the column two more times and buffer A was used for three
404 additional washes. Following wash cycles, the magnets were detached from the column, and
405 500 µL of buffer A was pipetted into the column. The plunger provided with the column was then
406 to provide additional force to collect all of the magnetosomes. Some of the cell lysate from each
407 sample was also saved as a control. Next, a Bradford assay was conducted on all samples to

408 determine the protein concentration, and if necessary, samples were concentrated during this
409 stage. Finally, all samples were trypsin-digested as previously described[17] to prepare them for
410 liquid chromatography-mass spectrometry, as detailed below.
411
412 **Liquid chromatography-mass spectrometry**
413 Trypsin-digested protein samples were each analysed in triplicate using an Acquity M-
414 class ultra-performance liquid chromatography (UPLC) system that was connected in line with a
415 Synapt G2-Si mass spectrometer (Waters, Milford, MA) as described elsewhere[17]. Data
416 acquisition and analysis were performed using MassLynx (version 4.1, Waters) and Progenesis
417 QI for Proteomics software (version 4.2, Waters Nonlinear Dynamics). Data were searched
418 against the *Desulfovibrio magneticus* strain RS-1 translated protein database to identify
419 peptides[41].
420
421 **Plasmid and cloning and deletion**
422 All plasmids used in this study for generating deletions and for their complementations in
423 RS-1, as well as for plasmids used in the BACTH assays, are listed in Supplemental table 3. In-
424 frame deletion vectors targeting *mad10*, *mad20*, *mad23*, *mad25*, *mad26, mad28* and *mamK*
425 were constructed by amplifying upstream and downstream homology regions of RS-1 genomic
426 DNA, using the primers listed in Supplementary Table 3. The homology regions were then
427 inserted into the XbaI site of pAK1127 using the Gibson cloning method. The P*npt -strAB*
428 cassette was subsequently inserted between the upstream and downstream homology regions
429 of the deletion vector. Plasmids were transformed into E. coli WM3064 and then transferred to
430 *D. magneticus* RS-1 using conjugation methods as described previously [13]. Allelic replacement
431 of *mad10, mad20, mad23, mad25, mad26, mad28* or *mamK* with *strAB* was achieved with
432 streptomycin selection and using two counterselections, 5-Flurouracil and sucrose. All deletions
433 were confirmed by PCR followed by full genomic Illumina sequencing using SeqCenter
434 (https://www.seqcenter.com).
435 To generate plasmids used to complement deletion strains, the genes *mad10*, *mad20*,
436 *mad23*, *mad25*, *mad26, mad28* and *mamK* were individually amplified using primers listed in
437 Supplemental table 4 and were cloned into pAK906 (containing the *npt* promoter) and pAK907
438 (containing a *mamA* promoter) using Gibson assembly. Both complementation plasmids for
439 each gene were tested by transformation into the respective RS-1 deletion strain. Each strain,
440 containing different versions of the complementation plasmid, was grown in liquid culture and
441 evaluated by C_{mag} measurements and TEM to determine which provided the best

442 complementation. The plasmid that most effectively restored the phenotype was selected for
443 further experiments.
444 To generate plasmids used in the BACTH studies, *mad10, mad20, mad23, mad25,*
445 *mad26, mad28* and *mamK* were either synthesized by Twist Bioscience
446 (https://www.twistbioscience.com) or PCR amplified using the primers listed in Supplementary
447 Table 4 and were cloned into pKT25 or pKNT25 (the N or the C-termini of the T25 fragment)
448 and pUT18 or pUT18C (the N or the C-termini of the T18 fragment) vectors in frame with the
449 T25 and T18 fragment open reading frames by Gibson assembly.
450
451 **Biomineralization time course using hydrogen**
452 RS-1 strains were grown at 30°C anaerobically, as described above. Initial cultures were
453 all grown with medium infused with 10% hydrogen and headspace was purged again with 10%
454 hydrogen after inoculation. All hydrogen cultures were grown on a wheel in the incubator.
455 Additionally, all cultures were transferred for supplementary growth into hydrogen tubes to
456 ensure the removal of all magnetosomes. Varying volumes (1mL, 0.5 mL, 0.2 mL, and 0.1 mL)
457 of hydrogen grown cultures were transferred into nitrogen-infused medium, aiming to capture all
458 stages of biomineralization more effectively. Optical density and magnetic response via C_{mag}
459 was monitored throughout growth as previously described [12] and at different stages of
460 biomineralization samples were saved for TEM imaging. The progression of biomineralization
461 stages was tracked using C_{mag}, with values ranging from 1.05 to 1.10 classified as early stages,
462 1.15 to 1.20 as middle stages, and 1.3 to 1.6 as late stages.
463
464 **Bacterial adenylate cyclase two-hybrid (BACTH) assays**
465 The assay was performed as described in the Euromedex BACTH system kit manual. N-
466 and C-terminal T18 and T25 fusions of Mad10, Mad20, Mad23, Mad25, Mad26, Mad28 and
467 MamK proteins were constructed using plasmid pKT25, pKNT25, pUT18C, and pUT18 in *E. coli*
468 K12 strain DH5-alpha. All plasmids were sequence-verified to show T18/T25 magnetosome
469 protein fusions were correct. The fusions were then co-transformed into competent *E. coli*
470 DHM1 cells (lacking endogenous adenylate cyclase activity) in all pairwise combinations, plated
471 on LB agar plates containing 100 µg/mL carbenicillin and 50 µg/mL kanamycin, and incubated
472 at 30 °C overnight. Several colonies of T18/T25 co-transformants were isolated and grown in LB
473 liquid medium with 100 µg/mL carbenicillin and 50 µg/mL kanamycin overnight at 30 °C with 220
474 rpm shaking. Overnight cultures were spotted on indicator plates containing minimal
475 M63/maltose medium with agar supplemented with 40 µg/mL X-gal, 50 µg/ml carbenicillin; and

476 25 µg/ml kanamycin. Plates were incubated 4 to 8 days at 30 °C before imaging. Bacteria
477 expressing interacting hybrid proteins will show blue, while bacteria expressing non-interacting
478 proteins will remain white. Different concentrations of IPTG (0, 0.1 mM and 0.5 mM) were tested
479 in the overnight culture as well as on the indicator plates with little to no difference. Therefore,
480 IPTG was not included in the final cultures and plates of this experiment.
481
482 **Electron microscopy**
483 Whole-cell TEM imaging was performed as described previously [15]. All TEM was done
484 using the Tecnai 12 at the EM-Lab at the University of California, Berkeley (https://em-
485 lab.berkeley.edu/EML/index.php). Magnetosomes were measured manually using ImageJ. Cells
486 were also counted manually.
487
488 **Acknowledgement**
489 A.K. and V.V.R. are supported through the National Institute of General Medical Sciences
490 (R35GM127114). The QB3/Chemistry Mass Spectrometry Facility at the University of California,
491 Berkeley received support from the National Institutes of Health (grant 1S10OD020062-01).
492 Additionally, V.V.R. was supported through the Genetics Training Grant, which receives funds
493 from the National Institutes of Health (Grant #: 1T32GM132022). Thank you to the staff at the
494 University of California Berkeley Electron Microscope Laboratory for advice and assistance in
495 electron microscopy.
496
497

Figures:

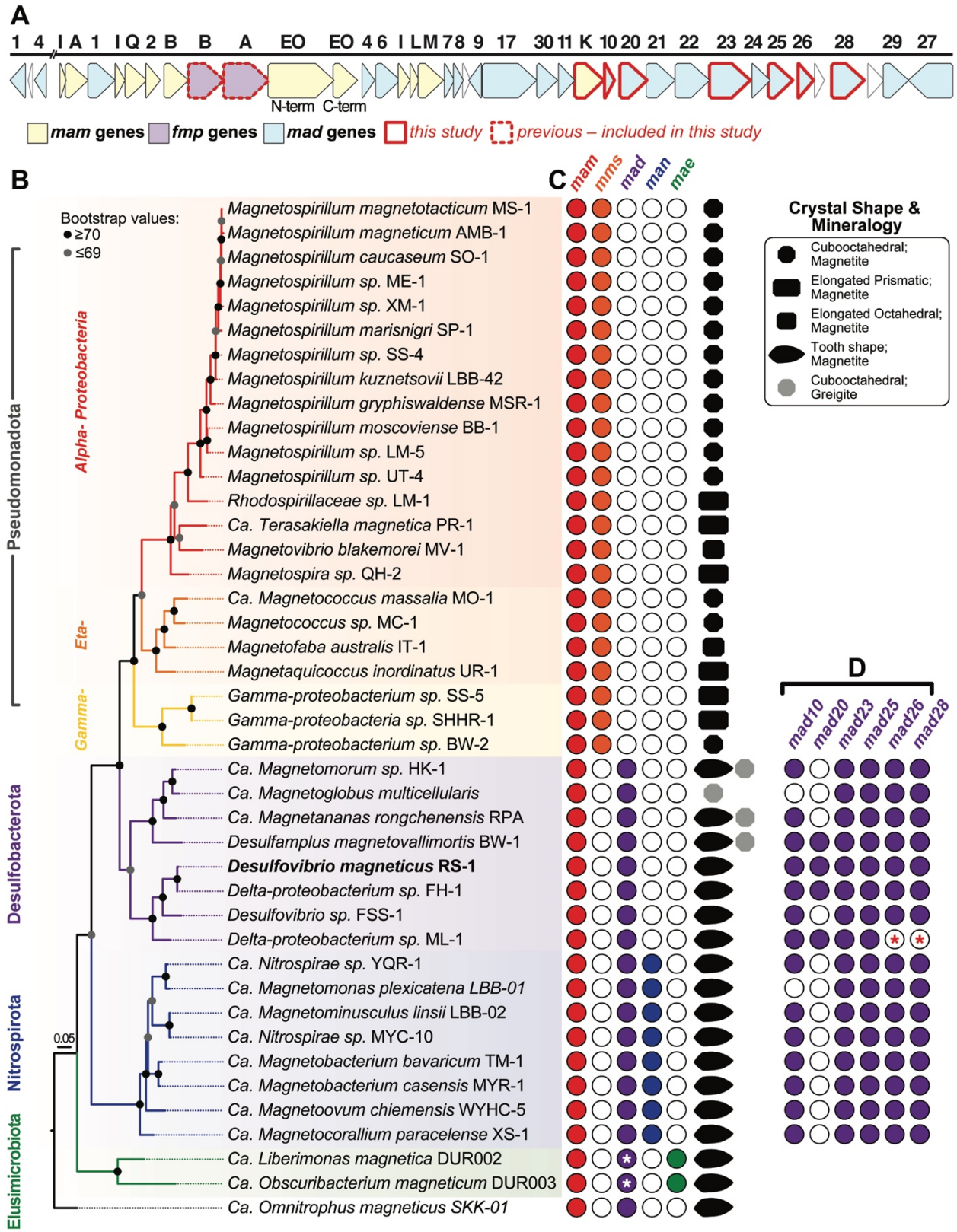
A
1 4 I A 1 I Q 2 B B A EO EO 4 6 I LM 7 8 9 17 30 11 K 10 20 21 22 23 24 25 26 28 29 27
N-term C-term
mam genes
fmp genes
mad genes
this study
previous – included in this study
B
C
mam
mms
mad
man
mae
Bootstrap values:
≥70
≤69
Pseudomonadota
Alpha- Proteobacteria
Eta-
Gamma-
Desulfobacterota
Nitrospirota
Elusimicrobiota
0.05
Magnetospirillum magnetotacticum MS-1
Magnetospirillum magneticum AMB-1
Magnetospirillum caucaseum SO-1
Magnetospirillum sp. ME-1
Magnetospirillum sp. XM-1
Magnetospirillum marisnigri SP-1
Magnetospirillum sp. SS-4
Magnetospirillum kuznetsovii LBB-42
Magnetospirillum gryphiswaldense MSR-1
Magnetospirillum moscoviense BB-1
Magnetospirillum sp. LM-5
Magnetospirillum sp. UT-4
Rhodospirillaceae sp. LM-1
Ca. Terasakiella magnetica PR-1
Magnetovibrio blakemorei MV-1
Magnetospira sp. QH-2
Ca. Magnetococcus massalia MO-1
Magnetococcus sp. MC-1
Magnetofaba australis IT-1
Magnetaquicoccus inordinatus UR-1
Gamma-proteobacterium sp. SS-5
Gamma-proteobacteria sp. SHHR-1
Gamma-proteobacterium sp. BW-2
Ca. Magnetomorum sp. HK-1
Ca. Magnetoglobus multicellularis
Ca. Magnetananas rongchenensis RPA
Desulfamplus magnetovallimortis BW-1
Desulfovibrio magneticus RS-1
Delta-proteobacterium sp. FH-1
Desulfovibrio sp. FSS-1
Delta-proteobacterium sp. ML-1
Ca. Nitrospirae sp. YQR-1
Ca. Magnetomonas plexicatena LBB-01
Ca. Magnetominusculus linsii LBB-02
Ca. Nitrospirae sp. MYC-10
Ca. Magnetobacterium bavaricum TM-1
Ca. Magnetobacterium casensis MYR-1
Ca. Magnetoovum chiemensis WYHC-5
Ca. Magnetocorallium paracelense XS-1
Ca. Liberimonas magnetica DUR002
Ca. Obscuribacterium magneticum DUR003
Ca. Omnitrophus magneticus SKK-01
Crystal Shape & Mineralogy
Cubooctahedral; Magnetite
Elongated Prismatic; Magnetite
Elongated Octahedral; Magnetite
Tooth shape; Magnetite
Cubooctahedral; Greigite
D
mad10
mad20
mad23
mad25
mad26
mad28

501 **Figure 1.** *Phylogenetic tree of MTB with their magnetosome gene composition and*
502 *magnetosome crystal shape*
503 (A) Magnetosome gene cluster in RS-1. All *mam* genes are in yellow, all *mad* genes are in blue
504 and *fmp* genes are in purple. Genes outlined in red (*mamK*, *mad10*, *mad20*, *mad23*, *mad25*,
505 *mad26* and *mad28*) were the focus of this study. Outlined in dotted red (*fmpA* and *fmpB*) are
506 genes mutated in a previous study[12], but examined further in this study. (B) 16S maximum
507 likelihood tree. MAFFT was used for alignment of 16S genes. Maximum likelihood tree was built
508 using PhyML Tree[39] with GTR substitution model and 1000 bootstraps. (C) For each MTB
509 species the classification of the type of magnetosome genes (*mam*, *mms*, *mad*, *man* or *mae*)
510 are provided as well as the magnetosome mineral composition and shape. White asterisks
511 indicate the potential presence of *mad* genes, which were previously reported as missing[8] (*see*
512 *Supplemental Figure S3-B*). (D) Deep-branching MTB species that contain the *mad* genes
513 studied here. Red asterisks represent uncertainty due to a lack of a completed genome on
514 NCBI. *Supplemental table 1* contains all the data (NCBI genome IDs, 16S gene ID and
515 references) used to generate the phylogenetic tree (B), magnetosome gene information (A, C &
516 D), and literature with crystal TEM images and chemical composition (C).
517

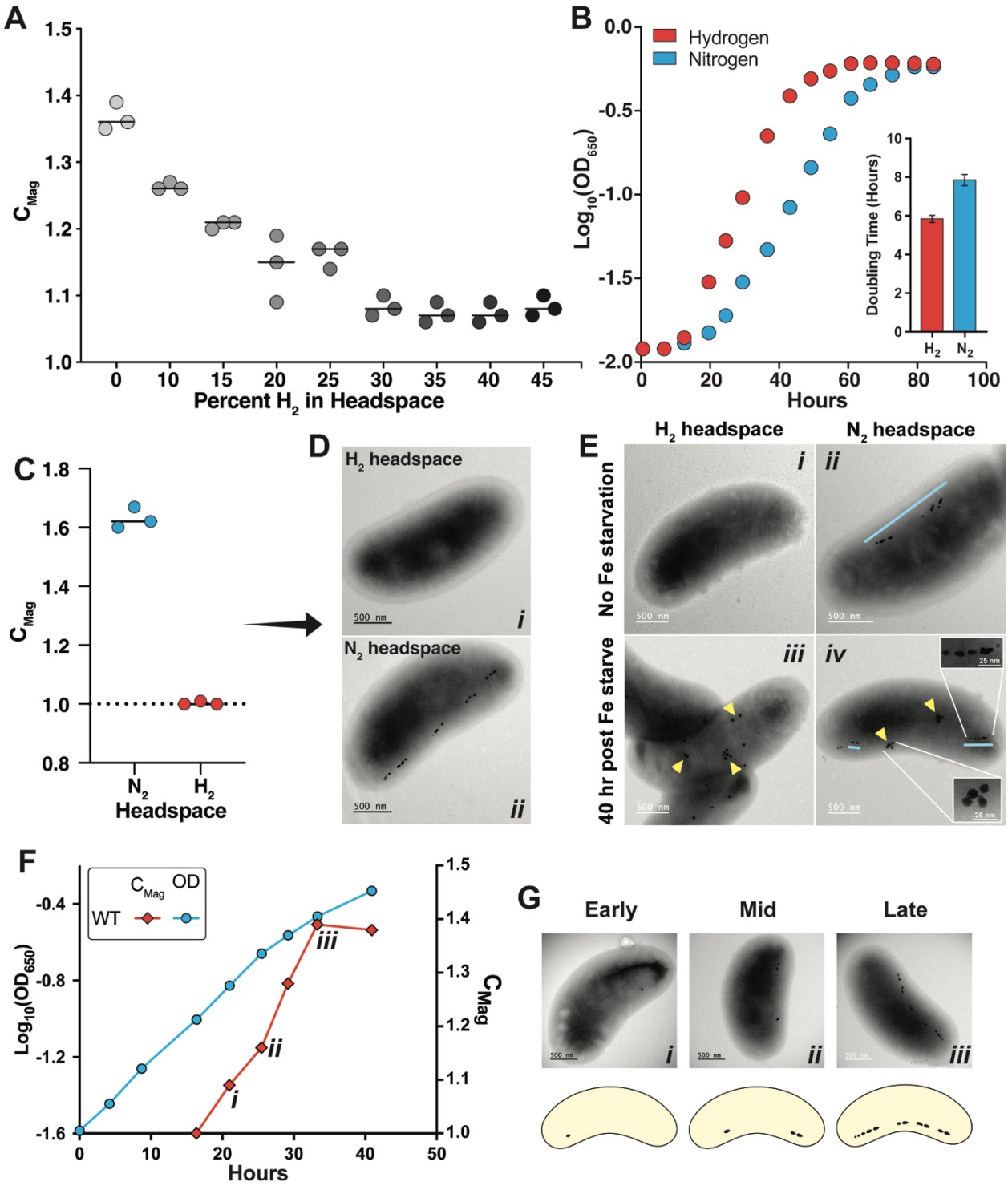

Figure 2. *Hydrogen inhibits magnetosome synthesis but not ferrosome production*

(A) Different concentration of hydrogen gas was added to the headspace and the magnetic response, C_{mag} was measured over growth. (B) Growth curve of WT RS-1 grown with nitrogen (blue) or hydrogen (orange) in the headspace. Inlet graph shows the doubling time for both

523 conditions. (C) RS-1 grown spinning on a wheel with either nitrogen (blue) or hydrogen
524 (orange). C_{mag} values indicate no magnetic response for cultures grown with hydrogen in the
525 headspace. (D) TEM images of cultures from (C). (E) Initial cultures were either grown with or
526 without iron to simulate iron starvation. Pre-cultures were transferred into either hydrogen or
527 nitrogen conditions. (E*i*) TEM image of a cell grown in hydrogen with no iron starvation, (E *ii*)
528 TEM image of a cell grown in nitrogen with no iron starvation, and (E *iii* and *iv*) are TEM images
529 after iron starvation for cells grown in hydrogen (*iii*) or nitrogen (*iv*). Blue lines indicate
530 magnetosomes and yellow triangles point to ferrosomes. (F) Growth curve (blue line) of a
531 culture transitioning from hydrogen to nitrogen conditions to initiate biomineralization. The C_{Mag}
532 curve (orange line) of the same culture demonstrates biomineralization initiation and
533 progression during growth. (F *i-iii*) indicate time points at which samples were collected for TEM
534 imaging in (G *i-iii*).
535

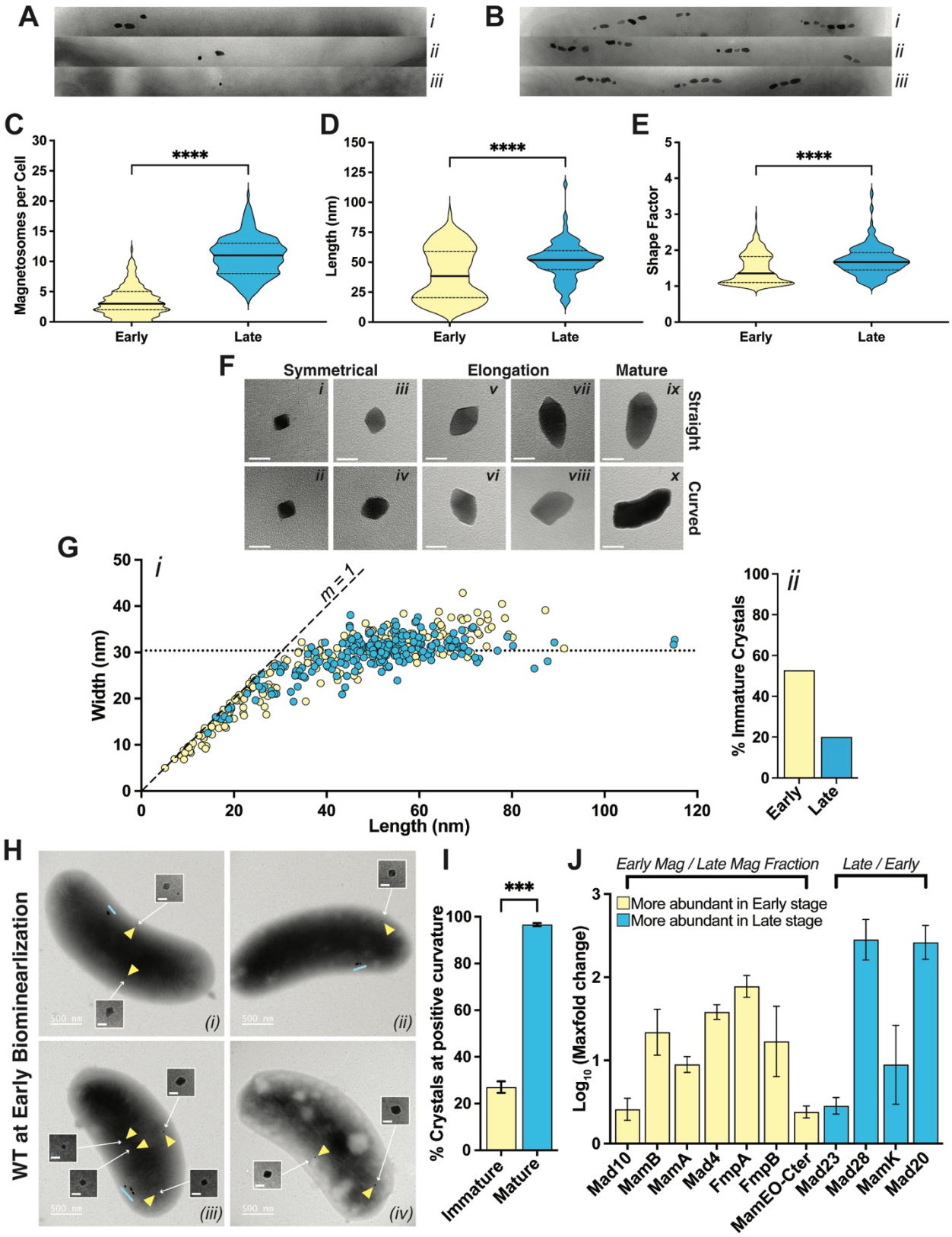

536

537 **Figure 3.** *Proteomic analysis of magnetosome proteins at different stages of biomineralization*

538 (A-B) TEM images of chains representing early and late stages of biomineralization. (C) Violin
539 plots depicting the number of magnetosomes per cell for cells in early and late stages of
540 biomineralization. (D) Violin plots illustrating measurements of magnetosome length and (E)
541 shape factor (length/width) for crystals found in early and late stages of biomineralization, n=212
542 for early stages and n=214 for late stages. (F) TEM images of RS-1 magnetosomes at different
543 stages of growth. All scale bars are 25 nm. (G) Each point is the measurement of the length and
544 width of one crystal from WT (AK80). Yellow dots represent crystals from cells at early stages of
545 biomineralization. Blue dots represent crystals from cells at late stages of biomineralization. The
546 dotted line represents the median width of crystals from late stages of biomineralization. Dashed
547 line shows a slope (*m*) of 1. (H) TEM images of early stage biomineralization of WT cells. Yellow
548 triangles point to immature crystals that are included as zoomed-in images in the inset. Blue line
549 indicates mature magnetosomes. The white scale bars for the zoomed-in crystals are all 25 nm.
550 (I) The proportion of magnetosomes positioned at the positive curvature of the cell for both
551 immature (yellow bar) and mature (blue bar) crystals during this stage, 140 cells counted; n=254
552 immature crystals, and n=394 mature crystals. (J) The $\log_{10}$ maximum fold change of
553 magnetosome protein abundance detected in the crystal fraction at different stages of
554 biomineralization. Yellow bars represent proteins more abundant at the early stage and blue
555 bars represent proteins more abundant at the late stage of biomineralization.
556

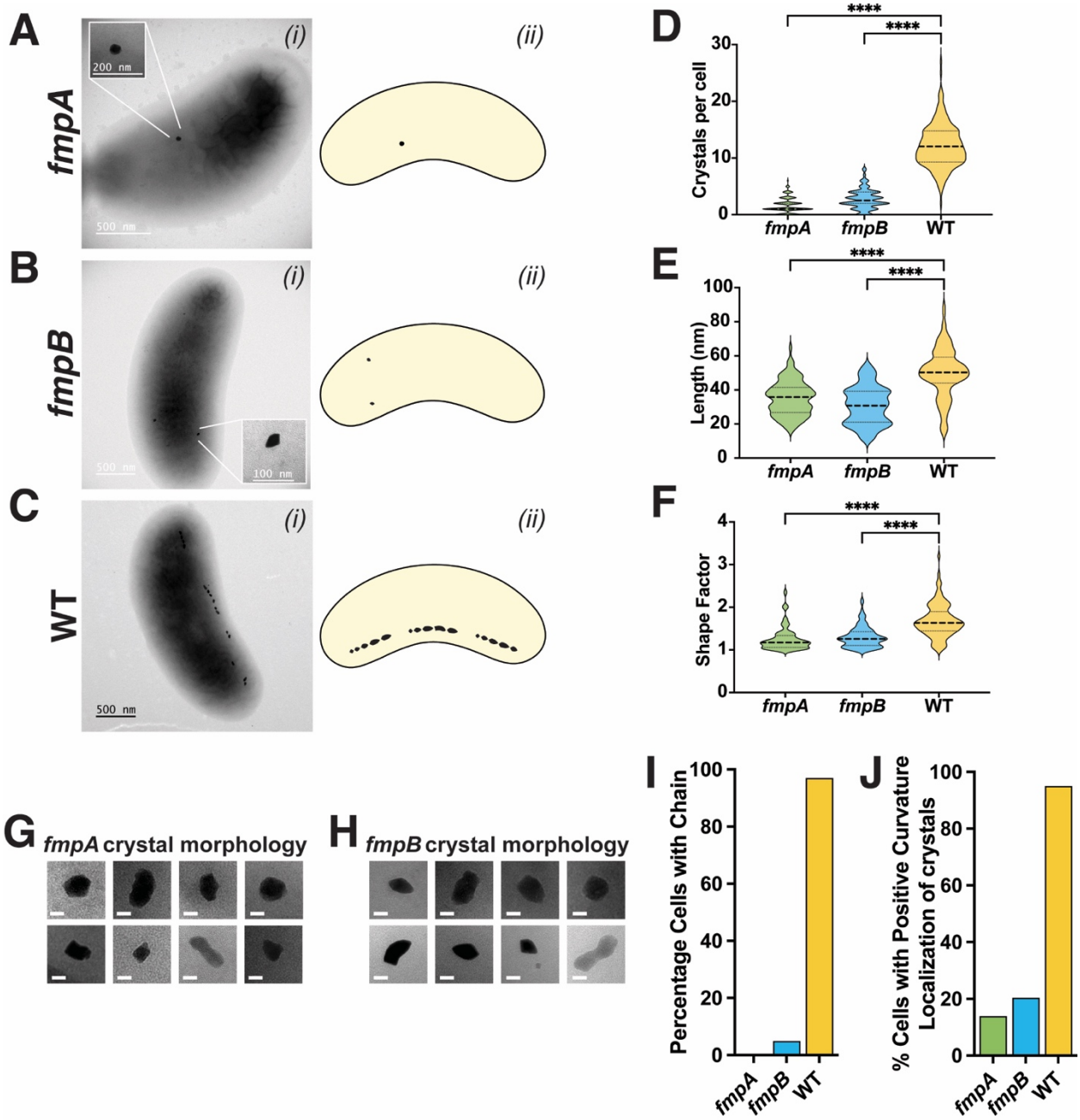

Figure 4. *Characterization of fmpA and fmpB mutants*

A-C) (*i*) TEM images of *fmpA* and *fmpB* mutant strains (scale bars 500 nm for main image and 100 nm for inset). (*ii*) Cartoon diagram of each strain. (D) Violin plots depicting the number of crystals per cell for each strain. (E) Violin plots illustrating measurements of magnetosome length, and (F) shape factor (length/width) for crystals in each strain. Data for (D), (E), and (F) are based on n=200 per strain. (G-H) Crystal morphology for each mutant, scale bars are 25 nm. (I) Percentage of cells exhibiting a chain phenotype, defined as having more than one

crystal aligned in a row, for each strain. (J) Percent of cells with crystals located at the positive curvature in the cell. (I-J) Over 200 cells were counted.

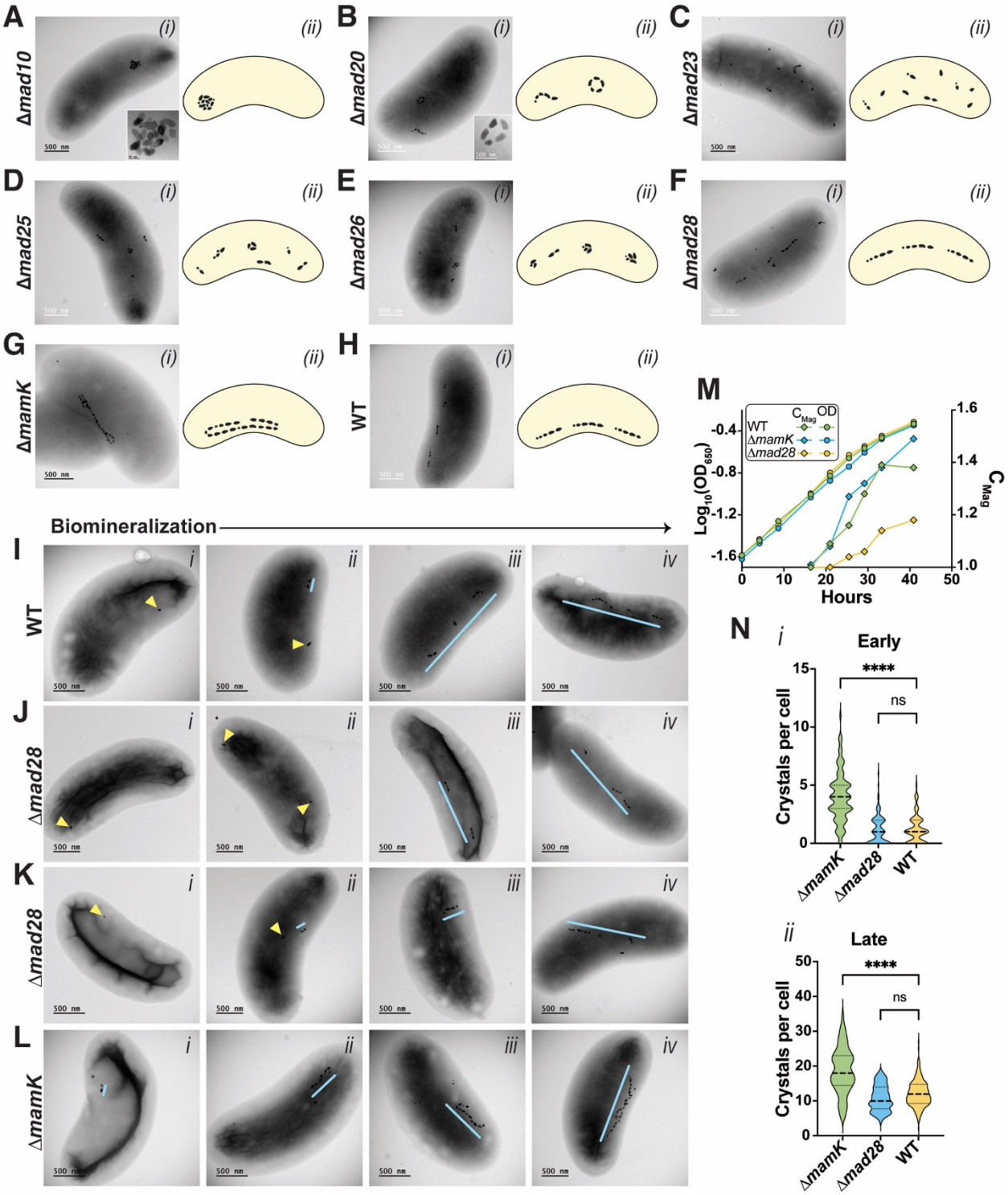

Figure 5. *Deletions of* mad *genes and mamK result in a variety of chain formation and localization defects*

(A-H) Phenotypes of different magnetosome gene deletion mutants and WT RS-1 with scale bars representing 500 nm. (*i*) is a TEM image ofor each strain and (*ii*) shows a cartoon diagram of representative magnetosome chain morphology. (I-L) TEM images of biomineralization time course of Δ*mad28*, Δ*mamK* and WT with scale bars representing 500 nm. Yellow triangles point at individual magnetosomes, whereas blue lines indicate chains or subchains of crystals. (I) Biomineralization time course of wildtype. (J) shows the phenotype for Δ*mad28* where the chain localizes to the mid-cell, whereas (K) shows the phenotype for Δ*mad28* where the chain localizes diagonally or transversally. (L) Biomineralization time course for Δ*mamK*, shows no subchains forming. (M) Growth curve and C_{mag} curve for WT, Δ*mad28* and Δ*mamK*. (N *i*) Violin plots depicting the number of magnetosomes per cell for WT, Δ*mad28* and Δ*mamK* at early stages of biomineralization, over 100 cells counted for each strain. (N *ii*) Violin plots illustrating the number of magnetosomes per cell for WT, Δ*mad28* and Δ*mamK* at late stages of biomineralization, over 100 cells counted for each strain.

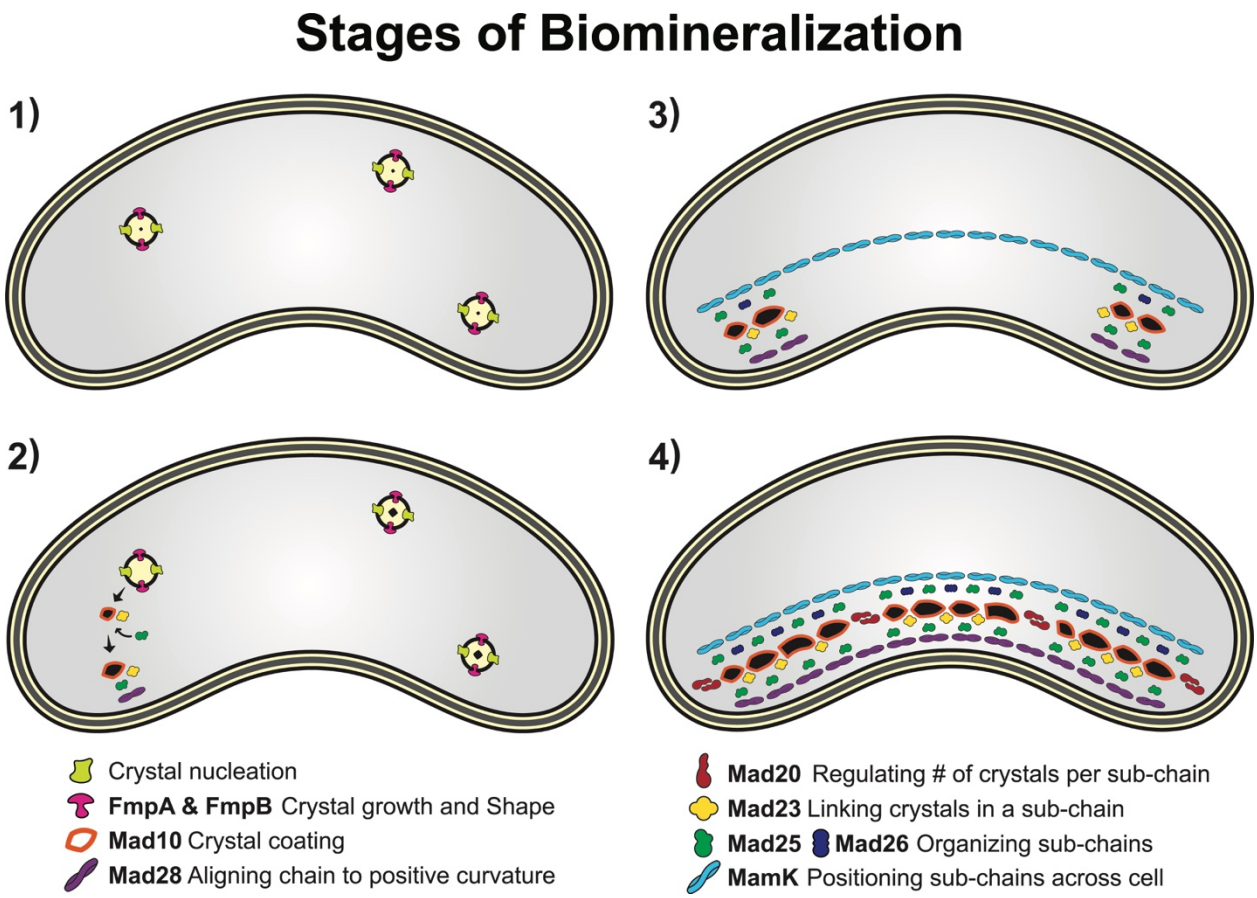

586 **Figure 6.** *Model of Magnetosome synthesis and chain organization in RS-1*
587 Model of the different stages of biomineralization in *Desulfovibrio magneticus* RS-1. ***Step 1:***
588 *Nucleation and Growth.* Biomineralization begins at nucleation sites randomly distributed within
589 the cell. ***Step 2:*** *Crystal Maturation and Localization.* Maturing crystals are transported to the
590 cell's positive curvature by a cohort of Mad proteins. ***Step 3:*** *Subchain Assembly.* As crystals
591 reach the positive curvature, the process shifts to organizing them into subchains. ***Step 4:***
592 *Chain Elongation and Centering.* Subchains are extended and aligned along the cell length by
593 MamK, while Mad28 ensures the chain remains localized at the positive curvature.
594

595 **References:**

596

597 1. Amor, M., Mathon, F. P., Monteil, C. L., Busigny, V. & Lefevre, C. T. Iron-biomineralizing
598 organelle in magnetotactic bacteria: function, synthesis and preservation in ancient rock
599 samples. *Environmental Microbiology* **22**, 3611–3632 (2020).
600 2. Wan, J. *et al.* Biomineralization in magnetotactic bacteria: From diversity to molecular
601 discovery-based applications. *Cell Reports* **43**, 114995 (2024).
602 3. Lefevre, C. T. & Bazylinski, D. A. Ecology, Diversity, and Evolution of Magnetotactic
603 Bacteria. *Microbiology and Molecular Biology Reviews* **77**, 497–526 (2013).
604 4. Amor, M. *et al.* Magnetotactic Bacteria Accumulate a Large Pool of Iron Distinct from Their
605 Magnetite Crystals. *Appl Environ Microbiol* **86**, e01278-20 (2020).
606 5. Vargas, G. *et al.* Applications of Magnetotactic Bacteria, Magnetosomes and Magnetosome
607 Crystals in Biotechnology and Nanotechnology: Mini-Review. *Molecules* **23**, 2438 (2018).
608 6. Lin, W. *et al.* Genomic expansion of magnetotactic bacteria reveals an early common origin
609 of magnetotaxis with lineage-specific evolution. *ISME Journal* **12**, 1508–1519 (2018).
610 7. Kolinko, I. *et al.* Biosynthesis of magnetic nanostructures in a foreign organism by transfer of
611 bacterial magnetosome gene clusters. *Nature Nanotech* **9**, 193–197 (2014).
612 8. Uzun, M. *et al.* Recovery and genome reconstruction of novel magnetotactic Elusimicrobiota
613 from bog soil. *The ISME Journal* **17**, 204–214 (2023).
614 9. Liu, P. *et al.* Key gene networks that control magnetosome biomineralization in
615 magnetotactic bacteria. *National Science Review* **10**, nwac238 (2023).
616 10. Sakaguchi, T., Burgess, J. G. & Matsunaga, T. Magnetite formation by a sulphate-reducing
617 bacterium. *Nature* **365**, 47–49 (1993).
618 11. Sakaguchi, T., Arakaki, A. & Matsunaga, T. Desulfovibrio magneticus sp. nov., a novel
619 sulfate-reducing bacterium that produces intracellular single-domain-sized magnetite
620 particles. *International Journal of Systematic and Evolutionary Microbiology* **52**, 215–221
621 (2002).
622 12. Rahn-Lee, L. *et al.* A Genetic Strategy for Probing the Functional Diversity of Magnetosome
623 Formation. *PLoS Genet* **11**, e1004811 (2015).
624 13. Grant, C. R., Rahn-lee, L. & Legault, K. N. Genome Editing Method for the Anaerobic
625 Magnetotactic. *Applied and Environmental Microbiology* **84**, 1–12 (2018).
626 14. Nakazawa, H. *et al.* Whole genome sequence of *Desulfovibrio magneticus* strain RS-1
627 revealed common gene clusters in magnetotactic bacteria. *Genome Res.* **19**, 1801–1808
628 (2009).

629 15. Byrne, M. E. *et al. Desulfovibrio magneticus* RS-1 contains an iron- and phosphorus-rich
630 organelle distinct from its bullet-shaped magnetosomes. *Proc. Natl. Acad. Sci. U.S.A.* **107**,
631 12263–12268 (2010).
632 16. Komeili, A., Vali, H., Beveridge, T. J. & Newman, D. K. Magnetosome vesicles are present
633 before magnetite formation, and MamA is required for their activation. *Proc. Natl. Acad. Sci.*
634 *U.S.A.* **101**, 3839–3844 (2004).
635 17. Grant, C. R. *et al.* Distinct gene clusters drive formation of ferrosome organelles in bacteria.
636 *Nature* **606**, 160–164 (2022).
637 18. Pi, H. *et al.* Clostridioides difficile ferrosome organelles combat nutritional immunity. *Nature*
638 **623**, 1009–1016 (2023).
639 19. Schüler, D., Uhl, R. & Bäuerlein, E. A simple light scattering method to assay magnetism in
640 *Magnetospirillum gryphiswaldense*. *FEMS Microbiology Letters* **132**, 139–145 (1995).
641 20. Li, J. *et al.* Crystal growth of bullet-shaped magnetite in magnetotactic bacteria of the
642 *Nitrospirae* phylum. *J. R. Soc. Interface.* **12**, 20141288 (2015).
643 21. Komeili, A., Li, Z., Newman, D. K. & Jensen, G. J. Magnetosomes Are Cell Membrane
644 Invaginations Organized by the Actin-Like Protein MamK. *Science* **311**, 242–245 (2006).
645 22. Pohl, A. *et al.* Decoding Biomineralization: Interaction of a Mad10-Derived Peptide with
646 Magnetite Thin Films. *Nano Lett.* **19**, 8207–8215 (2019).
647 23. Pohl, A. *et al.* Magnetite-binding proteins from the magnetotactic bacterium *Desulfamplus*
648 *magnetovallimortis* BW-1. *Nanoscale* **13**, 20396–20400 (2021).
649 24. Wan, J. *et al.* McaA and McaB control the dynamic positioning of a bacterial magnetic
650 organelle. *Nat Commun* **13**, 5652 (2022).
651 25. Abreu, N. *et al.* Interplay between Two Bacterial Actin Homologs, MamK and MamK-Like, Is
652 Required for the Alignment of Magnetosome Organelles in Magnetospirillum magneticum
653 AMB-1. *J Bacteriol* **196**, 3111–3121 (2014).
654 26. Toro-Nahuelpan, M. *et al.* Segregation of prokaryotic magnetosomes organelles is driven by
655 treadmilling of a dynamic actin-like MamK filament. *BMC Biol* **14**, 88 (2016).
656 27. Taoka, A. *et al.* Tethered Magnets Are the Key to Magnetotaxis: Direct Observations of
657 *Magnetospirillum magneticum* AMB-1 Show that MamK Distributes Magnetosome
658 Organelles Equally to Daughter Cells. *mBio* **8**, e00679-17 (2017).
659 28. Katzmann, E., Scheffel, A., Gruska, M., Plitzko, J. M. & Schüler, D. Loss of the actin-like
660 protein MamK has pleiotropic effects on magnetosome formation and chain assembly in
661 *Magnetospirillum gryphiswaldense*. *Molecular Microbiology* **77**, 208–224 (2010).

662 29. Awal, R. P. *et al.* Experimental analysis of diverse actin-like proteins from various
663 magnetotactic bacteria by functional expression in *Magnetospirillum gryphiswaldense*. *mBio*
664 **14**, e01649-23 (2023).
665 30. Liu, Y., Van Den Ent, F. & Löwe, J. Filament structure and subcellular organization of the
666 bacterial intermediate filament–like protein crescentin. *Proc. Natl. Acad. Sci. U.S.A.* **121**,
667 e2309984121 (2024).
668 31. Fields, S. & Song, O. A novel genetic system to detect protein–protein interactions. *Nature*
669 **340**, 245–246 (1989).
670 32. Müller, F. D., Schüler, D. & Pfeiffer, D. A Compass To Boost Navigation: Cell Biology of
671 Bacterial Magnetotaxis. *J Bacteriol* **202**, (2020).
672 33. Bickley, C. D., Wan, J. & Komeili, A. Intrinsic and extrinsic determinants of conditional
673 localization of Mms6 to magnetosome organelles in *Magnetospirillum magneticum* AMB-1. *J*
674 *Bacteriol* **206**, e00008-24 (2024).
675 34. Arakaki, A. *et al.* Comparative Subcellular Localization Analysis of Magnetosome Proteins
676 Reveals a Unique Localization Behavior of Mms6 Protein onto Magnetite Crystals. *J*
677 *Bacteriol* **198**, 2794–2802 (2016).
678 35. Chariaou, M. *et al.* Anisotropy of Bullet-Shaped Magnetite Nanoparticles in the
679 Magnetotactic Bacteria Desulfovibrio magneticus sp. Strain RS-1. *Biophysical Journal* **108**,
680 1268–1274 (2015).
681 36. Kovács, A. *et al.* Influence of crystal shape and orientation on the magnetic microstructure
682 of bullet-shaped magnetosomes synthesized by magnetotactic bacteria. *Geo-bio interfaces*
683 **1**, e1 (2024).
684 37. Chen, I.-M. A. *et al.* The IMG/M data management and analysis system v.7: content updates
685 and new features. *Nucleic Acids Research* **51**, D723–D732 (2023).
686 38. Katoh, K. & Standley, D. M. MAFFT multiple sequence alignment software version 7:
687 improvements in performance and usability. *Mol Biol Evol* **30**, 772–780 (2013).
688 39. Guindon, S. *et al.* New algorithms and methods to estimate maximum-likelihood
689 phylogenies: assessing the performance of PhyML 3.0. *Syst Biol* **59**, 307–321 (2010).
690 40. Constant Systems | Multi Cycle Cell Disruptor. *Constant Systems*
691 https://constantsystems.com/products/multi-cycle-cell-disruptor/.
692 41. Ehrlich, H., Bailey, E., Wysokowski, M. & Jesionowski, T. Forced Biomineralization: A
693 Review. *Biomimetics* **6**, 46 (2021).
694
695

696 **Extended Results:**

697

698 **Protein abundance during hydrogen-induced inhibition of magnetosome synthesis**

699 We investigated whether hydrogen affects magnetosome protein expression by comparing
700 proteomes of RS-1 cultures grown in hydrogen or nitrogen using liquid chromatography-mass
701 spectrometry. Most magnetosome gene cluster (MGC) proteins showed similar levels, except
702 Mad10, which was over 20 times more abundant in nitrogen (Supplemental Figure S8-B).
703 However, Mad10 is not responsible for magnetosome inhibition under hydrogen conditions, as
704 indicated by its magnetosome formation phenotype. In hydrogen-grown cells, hydrogenases, a
705 response regulator, a signaling protein, and the ferric uptake regulator, Fur, were more
706 abundant, while nitrogen-grown cells had higher levels of dehydrogenases and a carbon
707 storage regulator (Supplemental Figure S8 C-F). These findings suggest potential molecular
708 mechanisms for hydrogen's effect on magnetosome formation, warranting further investigation
709 in the future.

710

711 **Architecture of Chain organization proteins in RS-1**

712 For each chain organization gene deleted in RS-1, predicted protein structures were
713 modeled to visualize their structural features. Mad20, Mad25, and Mad26 all exhibited similar
714 protein structures, characterized by long coiled-coil filament-like regions (Supplemental Figure
715 S5 C-E), resembling the coiled-coil protein, Crescentin, found in *Caulobacter crescentus*[1].
716 These coiled-coil domains are predicted to facilitate strong protein-protein interactions, which
717 was supported by bacterial two-hybrid assays, where all three proteins interacted extensively
718 with each other as well as with other chain organization proteins (Supplemental Figure S2).
719 Mad10 and Mad23, in contrast, have much shorter coiled-coil regions (Supplemental Figure
720 S3A), which is also reflected in their 3D structural models (Supplemental Figure S5 A-B). While
721 Mad10 lacks additional predicted domains, previous studies suggest it contains a magnetite-
722 binding region[2]. Mad23, however, possesses a distinctive HEAT repeat domain in addition to its
723 small coiled-coil region (Supplemental Figure S5 B-ii). HEAT domains are typically associated
724 with protein-protein interactions, a hypothesis further supported by bacterial two-hybrid assays,
725 where Mad23 showed strong interactions with Mad10 and Mad25 (Supplemental Figure S2).

726 Both Mad28 and MamK are predicted to contain actin-like domains and share highly
727 similar predicted protein structures (Supplemental Figure S5 F-G). To further investigate their
728 relationship, we performed both 3D structural and protein sequence alignments. While the
729 sequence alignment revealed low similarity, the 3D structural alignment showed strong

730 alignment between the two proteins, suggesting that despite sequence divergence, their
731 structural similarities may indicate conserved functions. However, our genetic studies and
732 biomineralization time course analyses revealed distinct roles: MamK is essential for sub-chain
733 formation, while Mad28 is required for proper chain localization along the positive curvature
734 (Figure 5F-G). Additionally, the original *mad28* sequence from RS-1 in the NCBI database
735 before 2019 lacked the first 114 nucleotides or 38 amino acids, shown in green in Supplemental
736 Figure S5 H-J. However, this region is essential for restoring the wild-type phenotype in *mad28*
737 complementation experiments. Notably, this sequence is unique to Mad28 and does not align
738 with MamK in the 3D structural comparison (Supplemental Figure S5-H). This specific *mad28*
739 region is also present in Mad28 homologs from other deep-branching MTB, further supporting
740 its functional significance. Supplemental Figure S5-I highlights this region in green in MYR-1, a
741 deep-branching MTB from the *Nitrospirota* phylum.
742
743

744 **Extended data Figures:**

745

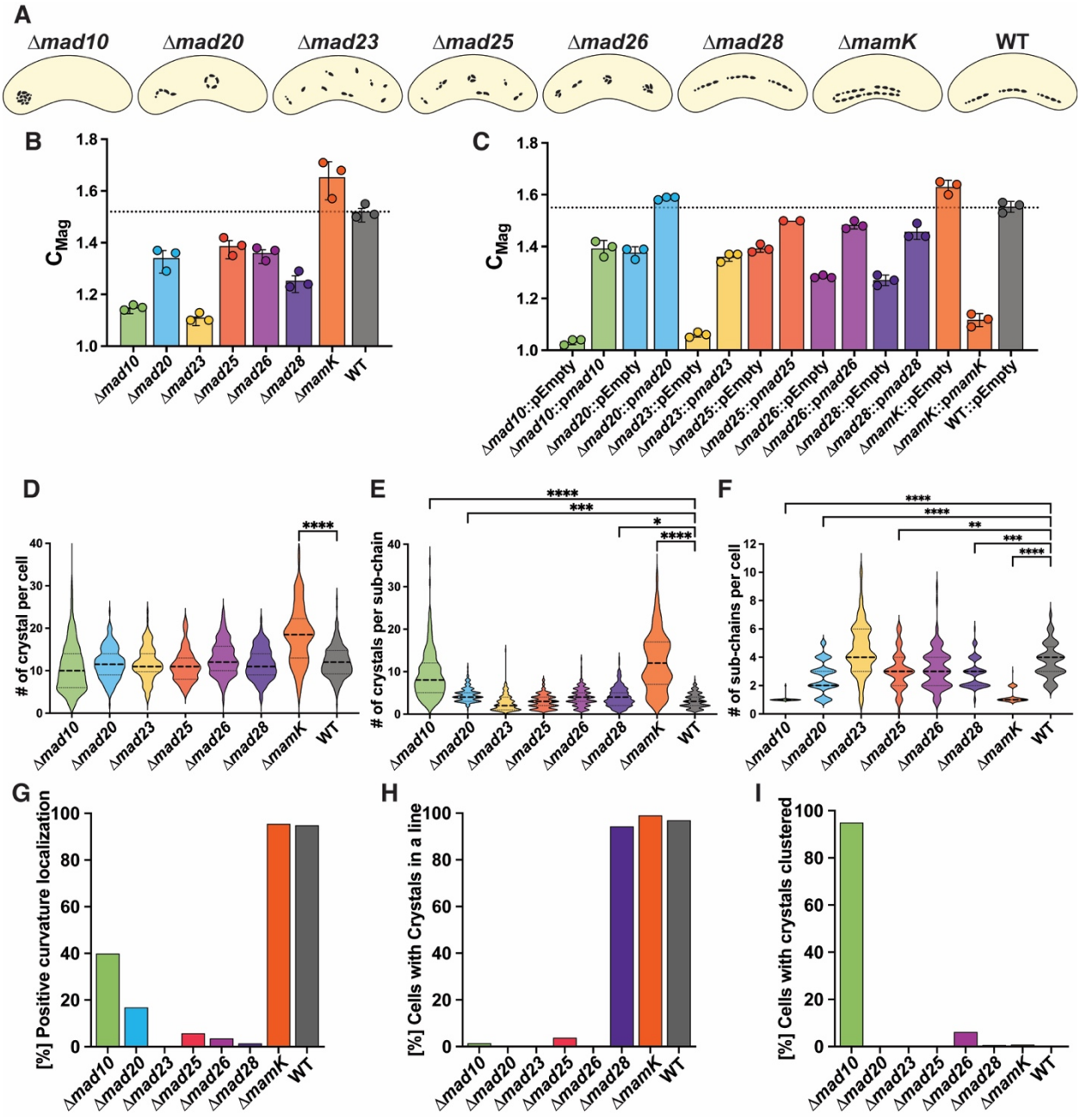

746

747 **Supplemental S1.** *Characterization of magnetosome gene deletions in RS-1*

748 (A) Cartoon diagram of representative phenotype of each strain. (B) C_{Mag} values for each strain,
749 with cultures grown in triplicate. No plasmids were present in the cells. Error bars indicate
750 standard deviation. (C) C_{Mag} values for each mutant with an empty plasmid and for each mutant
751 with a plasmid constitutively expressing the deleted gene. The WT strain carries only an empty
752 plasmid. The dotted line in (B) and (C) represents the average C_{Mag} of WT. (D) Violin plots

displaying the number of crystals per cell for each strain. (E) Violin plots illustrating the number of crystals per subchain for each strain. (F) Violin plots representing the number of subchains per cell for each strain. All statistical tests used on (D), (E), and (F) are stated in *Supplemental table 8*. (G-I) The percentage of cells exhibiting specific phenotypes, based on a count of 200 cells per strain. (G) The percentage of cells with crystals localized at the positive curvature of the cell, (H) shows the percentage of cells with magnetosomes displaying a chain phenotype, and (I) indicates the percentage of cells with all magnetosomes in the cell clustered together.

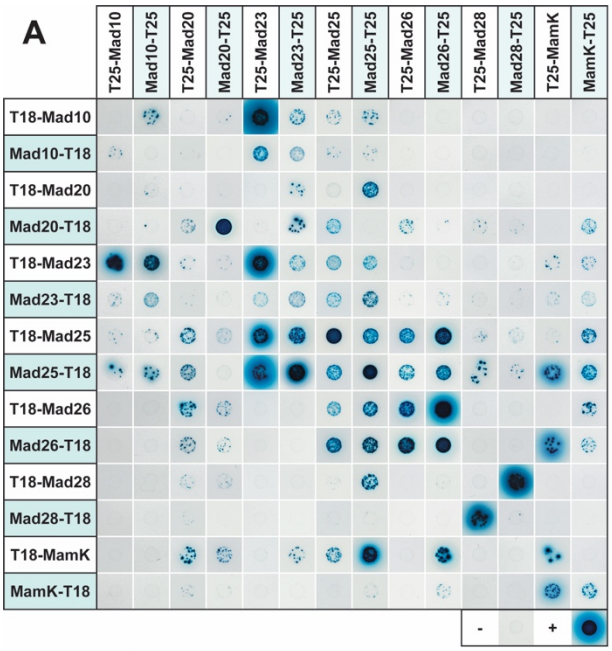

B

	T25-Mad10	Mad10-T25	T25-Mad20	Mad20-T25	T25-Mad23	Mad23-T25	T25-Mad25	Mad25-T25	T25-Mad26	Mad26-T25	T25-Mad28	Mad28-T25	T25-MamK	MamK-T25
T18-Mad10	-	++	-	-	+++	+	+	+	-	-	-	-	-	-
Mad10-T18	+	-	-	-	++	+	+	+	-	-	-	-	-	-
T18-Mad20	-	+	-	-	-	+	-	++	-	-	-	-	-	-
Mad20-T18	-	-	+	+++	-	++	+	-	+	-	+	+	-	+
T18-Mad23	+++	+++	+	+	+++	+	+	+	-	-	-	-	+	+
Mad23-T18	+	+	-	-	+	+	+	++	-	+	-	-	+	+
T18-Mad25	+	+	++	+	+++	++	+++	++	++	+++	+	+	-	++
Mad25-T18	+	++	++	-	+++	+++	++	+++	+	++	++	+	++	++
T18-Mad26	-	-	++	+	-	-	+	++	++	+++	-	-	-	++
Mad26-T18	-	-	++	+	-	-	++	++	+++	+++	-	-	++	+
T18-Mad28	-	-	+	+	-	-	-	++	-	-	-	+++	-	-
Mad28-T18	-	-	-	-	-	-	-	-	-	-	+++	-	-	-
T18-MamK	-	-	++	++	-	+	++	+++	-	++	-	-	++	-
MamK-T18	-	-	+	-	-	-	-	-	-	+	-	-	++	++

C

	Domains	Significant interactions
Mad10	Coiled-coil	10, **23**, 25
Mad20	Coiled-coil	**20**, 23, 25, 26, K
Mad23	Coiled, Heat	**10**, 20, **23**, **25**
Mad25	Coiled-coil	10, 20, 23, **25**, **26**, 28, **K**
Mad26	Coiled-coil	**25**, **26**, **K**
Mad28	Actin-like	25, **28**
MamK	Actin-like	23, **25**, **26**, **K**

*Bold are the most significant interactions

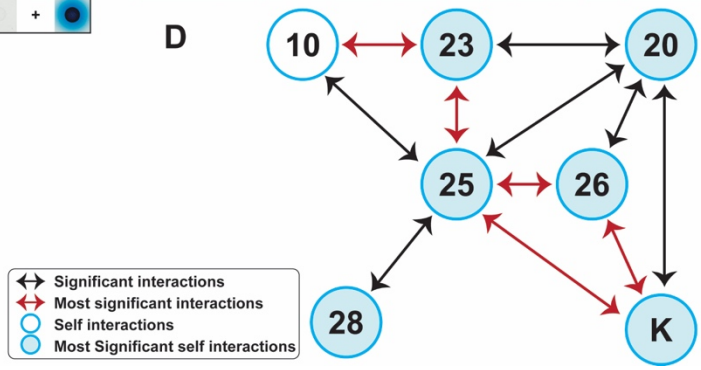

Supplemental S2. *Interactions of magnetosome chain organization proteins*

A Bacterial Adenylate Cyclase Two-Hybrid (BACTH) assay was conducted to assess interactions among magnetosome chain organization proteins—Mad10, Mad20, Mad23, Mad25, Mad26, Mad28, and MamK. Co-transformed E. coli DHM1 expressing T18- and T25-fusion proteins were spotted onto M63 maltose-mineral salts agar, where blue coloration indicates high β-galactosidase activity, signifying a positive interaction, while white indicates no interaction.

The positive control (leucine zipper) resulted in dark blue spots, while the negative controls (empty vector combinations) produced white spots, as expected. (A) Photographic images of spots for each interaction combination. (B) A table summarizing all interaction combinations, scored based on results from (A) and categorized by color intensity: dark blue spots indicate strong interaction (+++), medium blue spots represent moderate (++), light blue spots signify minor (+), and white denotes no interaction (-). (C) A table highlighting the most significant interactions. (D) A visual diagram illustrating these interactions: black arrows represent medium interactions, including bidirectional interactions (fusion with T25 and T18 interacting with their corresponding fusion partners), red arrows highlight strong bidirectional interactions, open blue circles indicate observed self-interactions, and filled blue circles denote strong self-interactions.

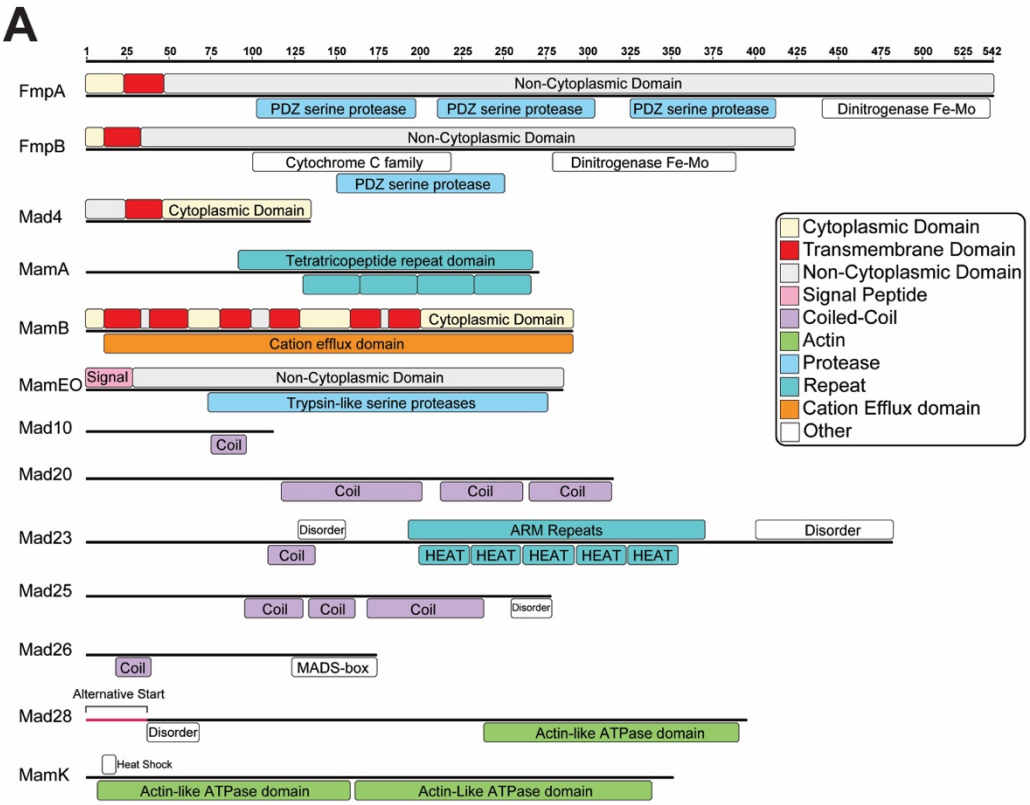

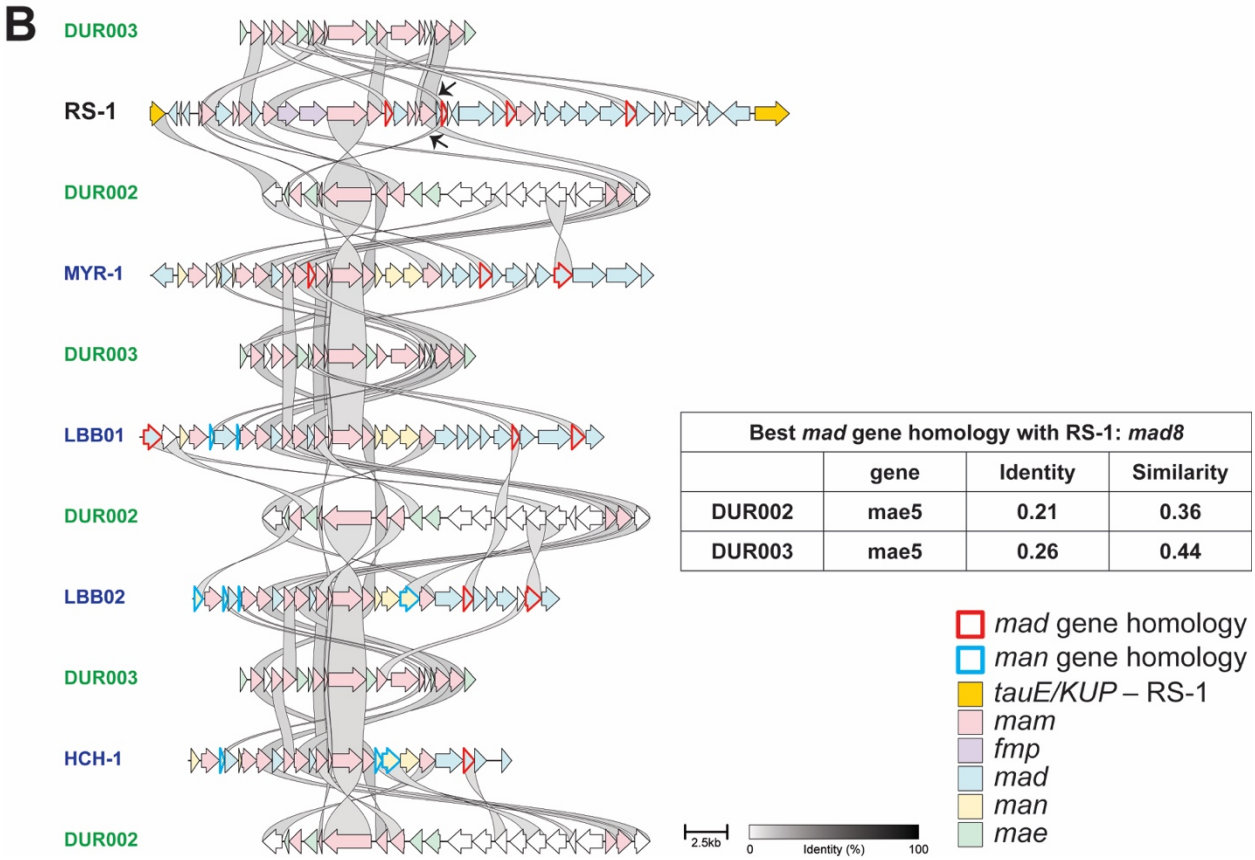

Best *mad* gene homology with RS-1: *mad8*			
	gene	Identity	Similarity
DUR002	mae5	0.21	0.36
DUR003	mae5	0.26	0.44

780 **Supplemental S3.** *Protein domains of magnetosome genes in this study and mad gene*
781 *comparisons between deep branching MTB.*
782 (A) Domains of proteins studied here. Protein domains were identified using InterPro [3] and
783 uploaded on to Geneious [4] to generate domain maps. Mad28 shows an alternative start site that
784 was not included in the original NCBI annotation and Δ*mad28* could only be complemented
785 when including the alternative start site. (B) Magnetosome gene cluster comparison between
786 DUR002 and DUR003 *(Elusimicrobiota)* and RS-1 *(Desulfobacterota* representative*),* and
787 between DUR002 and DUR003 and MYR-1, LBB01, LBB02, and HCH-1 *(Nitrospirota*
788 representatives*)*. This analysis is to indicate, while DUR002 and DUR003 are stated to not
789 contain any mad genes[5] they do have homologues to some *mad* genes. Magnetosome gene
790 clusters were extracted from genomes available on NCBI manually and Clinker[6] was used to
791 compare the MGCs. Genes outlined in red are *mad* genes that show some homology in either
792 DUR002 or DUR003. Genes outlined in blue are *man* genes that show some homology in either
793 DUR002 or DUR003. The table on the right shows the proportions of identity and similarity for
794 homology of *mad8*, which was found to have homologs in both DUR002 and DUR003. The
795 black arrows indicate the *mad8* homology on the comparison map. *mad4*, *mad11* and *mad24*
796 from RS-1 also had homologs, but only in DUR003. In addition, *mad24* has a homolog to
797 DUR003 in two *Nitrospirota* representatives, HCH-1 and LBB02.
798

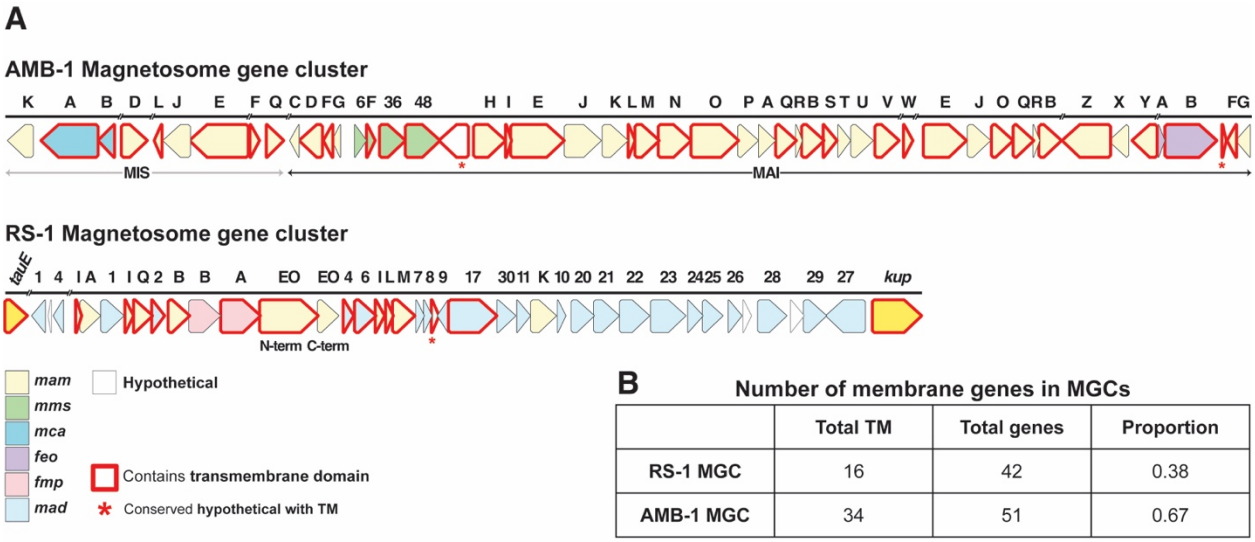

B Number of membrane genes in MGCs

	Total TM	Total genes	Proportion
RS-1 MGC	16	42	0.38
AMB-1 MGC	34	51	0.67

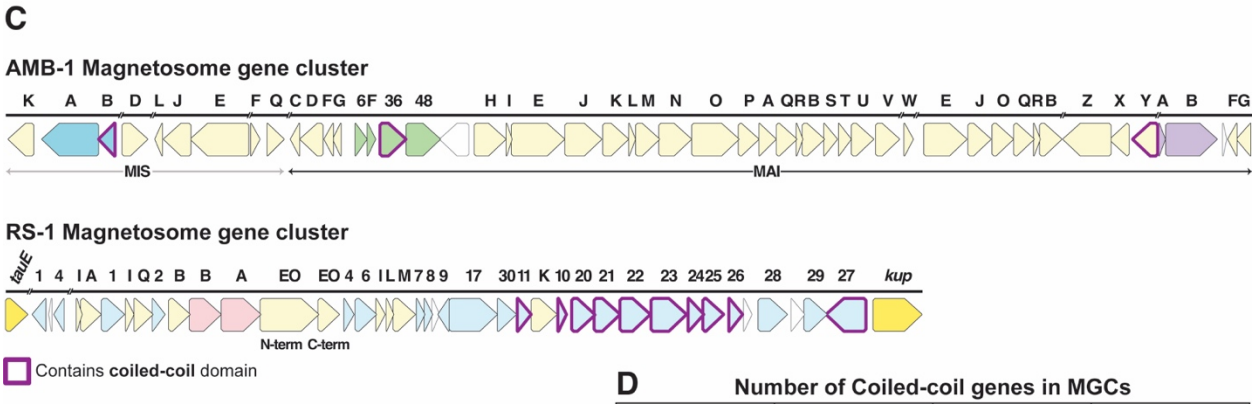

D Number of Coiled-coil genes in MGCs

	Total CC	Total genes	Proportion
RS-1 MGC	10	42	0.24
AMB-1 MGC	3	51	0.06

Supplemental S4. *Magnetosome gene cluster comparison between AMB-1 and RS-1.* (A) Magnetosome gene clusters in AMB-1 and RS-1. Genes highlighted in red encode for proteins with predicted transmembrane domains. (B) Table of the proportions of proteins with predicted transmembrane domains to all proteins encoded by the magnetosome gene clusters of AMB-1 and RS-1. TMHMM[7] was used to gather transmembrane domain predictions. (C) Magnetosome gene cluster of AMB-1 and RS-1 with genes encoding proteins with predicted coiled-coil domains highlighted in purple. (D) Table of the proportions of proteins with coiled-coil domains compared to all proteins in the MGC for AMB-1 and RS-1. DeepCoil[8] was used to obtain coiled-coil predictions.

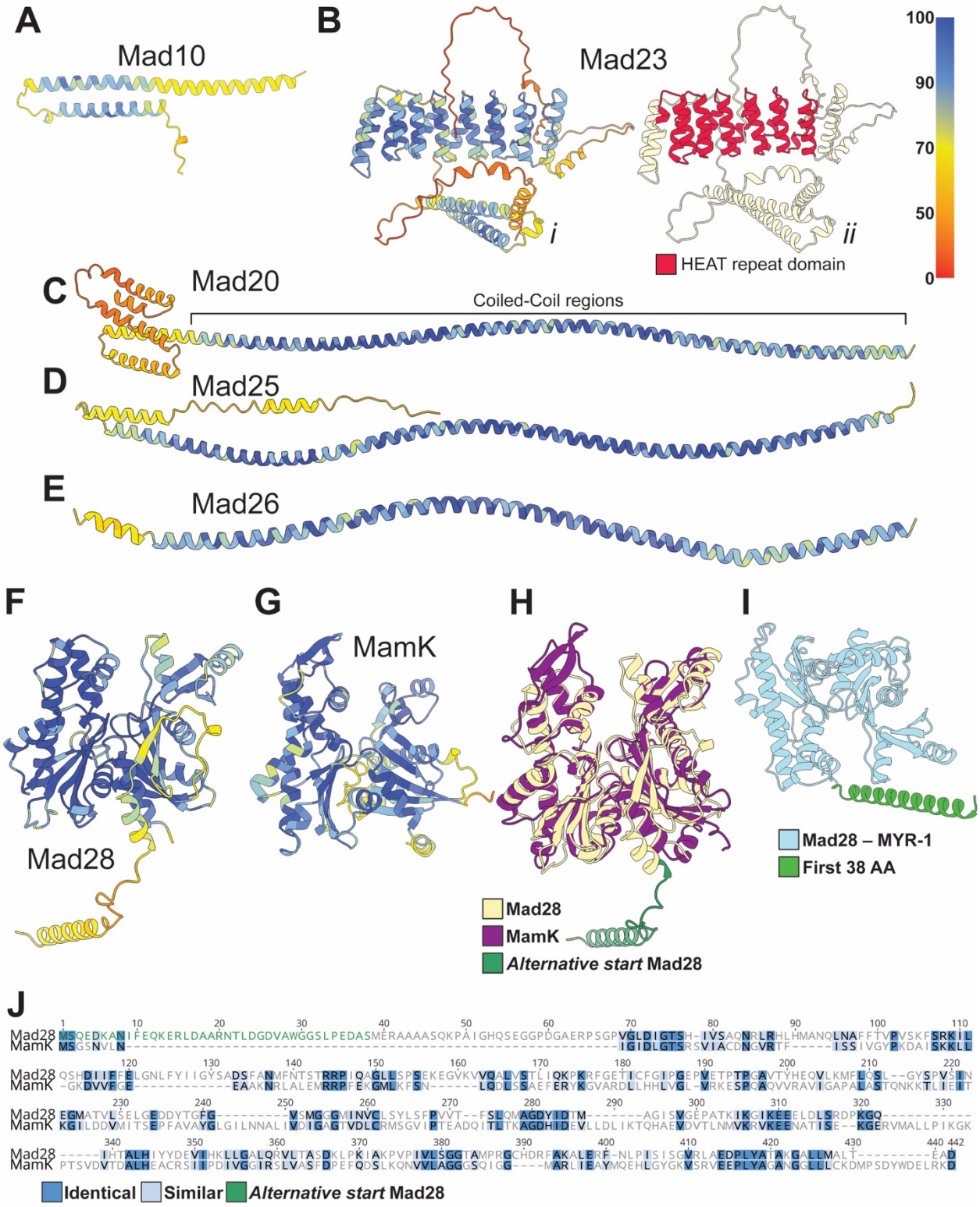

Supplemental S5. *Predicted 3D Structures of magnetosome proteins deleted in RS-1 and alignments of MamK and Mad28*

813 (A-I) Predicted protein structures of Mad proteins and MamK in this study were made with
814 Alphafold3[9] and visualized with ChimeraX[10]. 3D structures are colored according to Alphafold
815 confidence values, with blue at 100% confident and red 0% confidence. (B-*ii*) Indicates the
816 location of the HEAT domain (colored in red) in Mad23. (H) 3D alignment of protein structures of
817 Mad28 and MamK from RS-1. Protein structures were made with alphafold3 and then a 3D
818 alignment was preformed using ChimeraX[10]. Purple is the 3D predicted structure for MamK,
819 yellow is the predicted structure for Mad28 and green is the part of the structure that includes
820 the alternative start site for Mad28. Δ*mad28* would only complement with this sequence
821 included in the plasmid. (I) Predicted 3D structure of Mad28 from MYR-1, a deep-branching
822 MTB in the *Nitrospirota* phylum. The first 38 amino acids are highlighted in green to indicate
823 structural similarity to the corresponding region in RS-1's Mad28. (J) 2D protein sequence
824 alignment of MamK and Mad28 using MAFFT v7.490 plug-in on Geneious[4]. Blue highlighted
825 residues show similarities between sequences and dashes represent gaps. Green letters show
826 the sequence for the alternative start in Mad28.
827

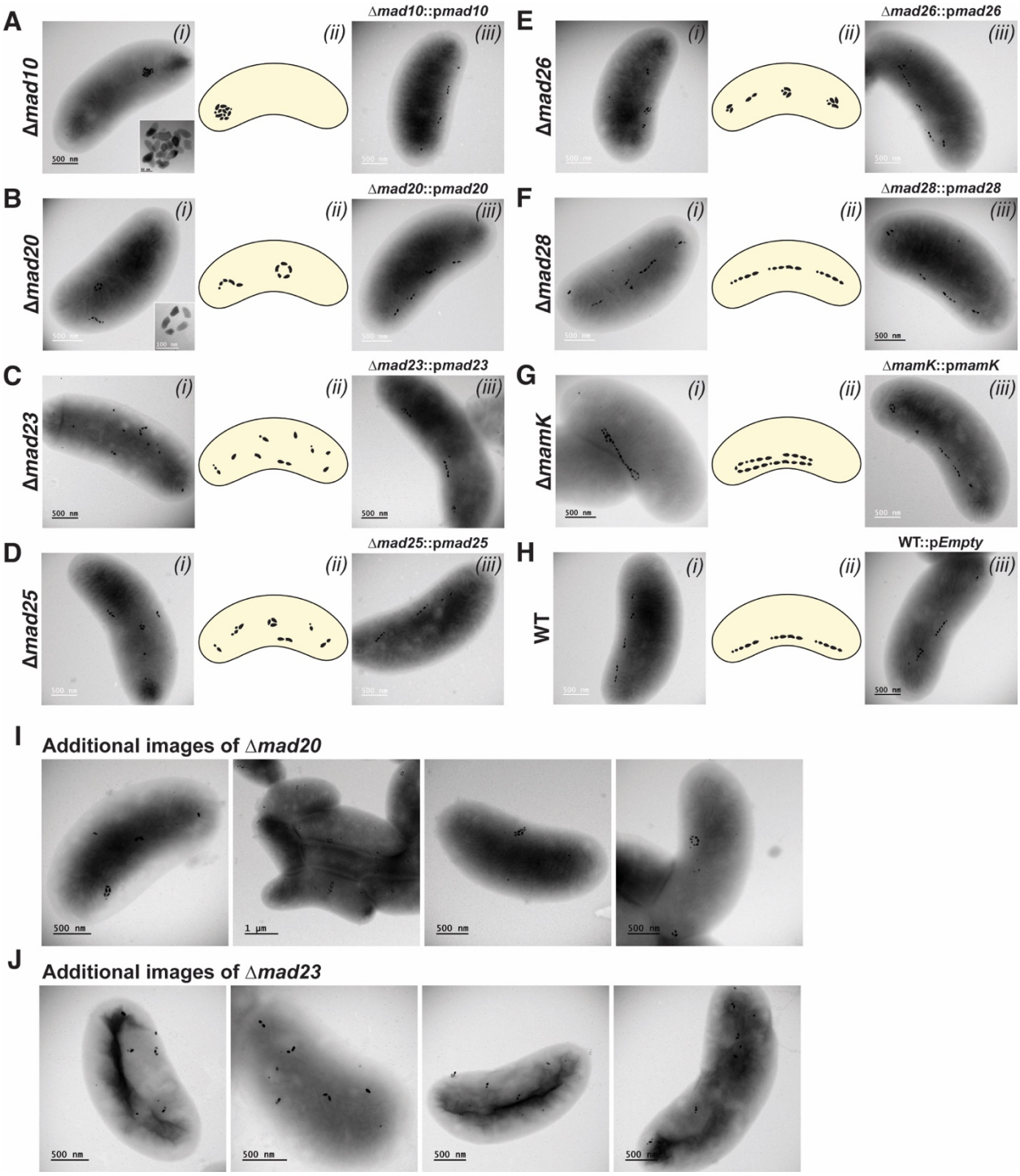

Supplemental S6. *TEM images of complementation of deletion mutants*

(A-G) TEM images of deletion mutants and their respective complementation strains in RS-1. All complementations were done by expressing the gene on a plasmid. (H) TEM images of WT and a WT control with an empty plasmid. (I) Additional TEM images of Δ*mad20* in RS-1. These images are to illustrate fewer subchains in each cell and more crystals per subchain in each cell

834 to complement the statistical data from Supplemental Figure S1. Perhaps rings form in this
835 mutant because subchains are too long, similar to the Δ*mamK* phenotype. (J) Additional TEM
836 images of Δ*mad23* in RS-1. These images are to illustrate the higher number of subchains in
837 each cell and fewer crystals per subchain in each cell to complement the statistical data from
838 Supplemental Figure S1. Subchains are more scattered in Δ*mad23*.
839

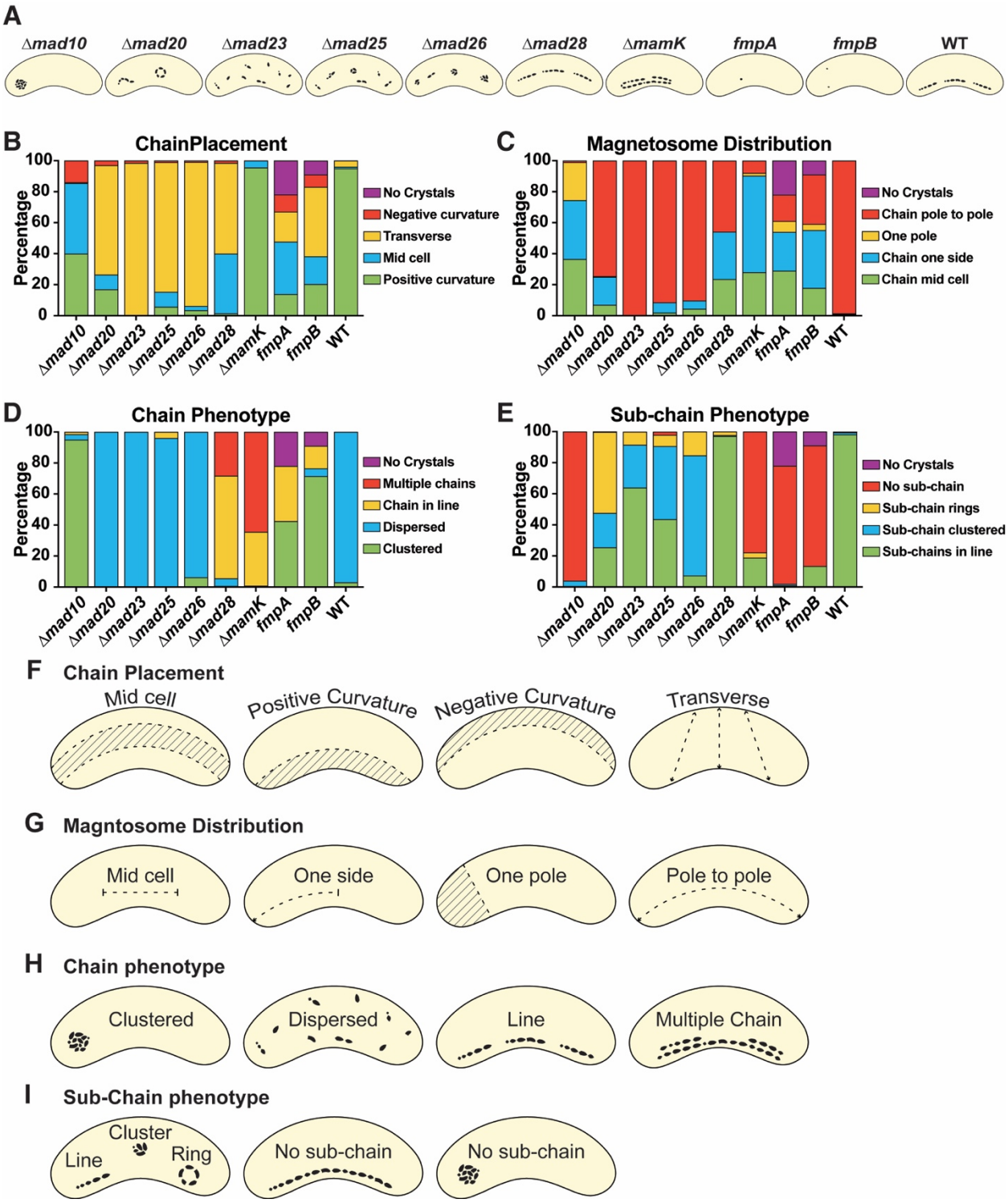

Supplemental S7. *Additional mutant phenotypes and magnetosome chain and subchain categories*

843 (A) Illustrations of the phenotypes of the different mutants in this study. (B-E) Additional
844 phenotype categories for all mutants. (F-I) Categories used to calculate mutant phenotypes in
845 Figure 4, Supplemental Figure S1, as well as (B-E) in this figure.
846

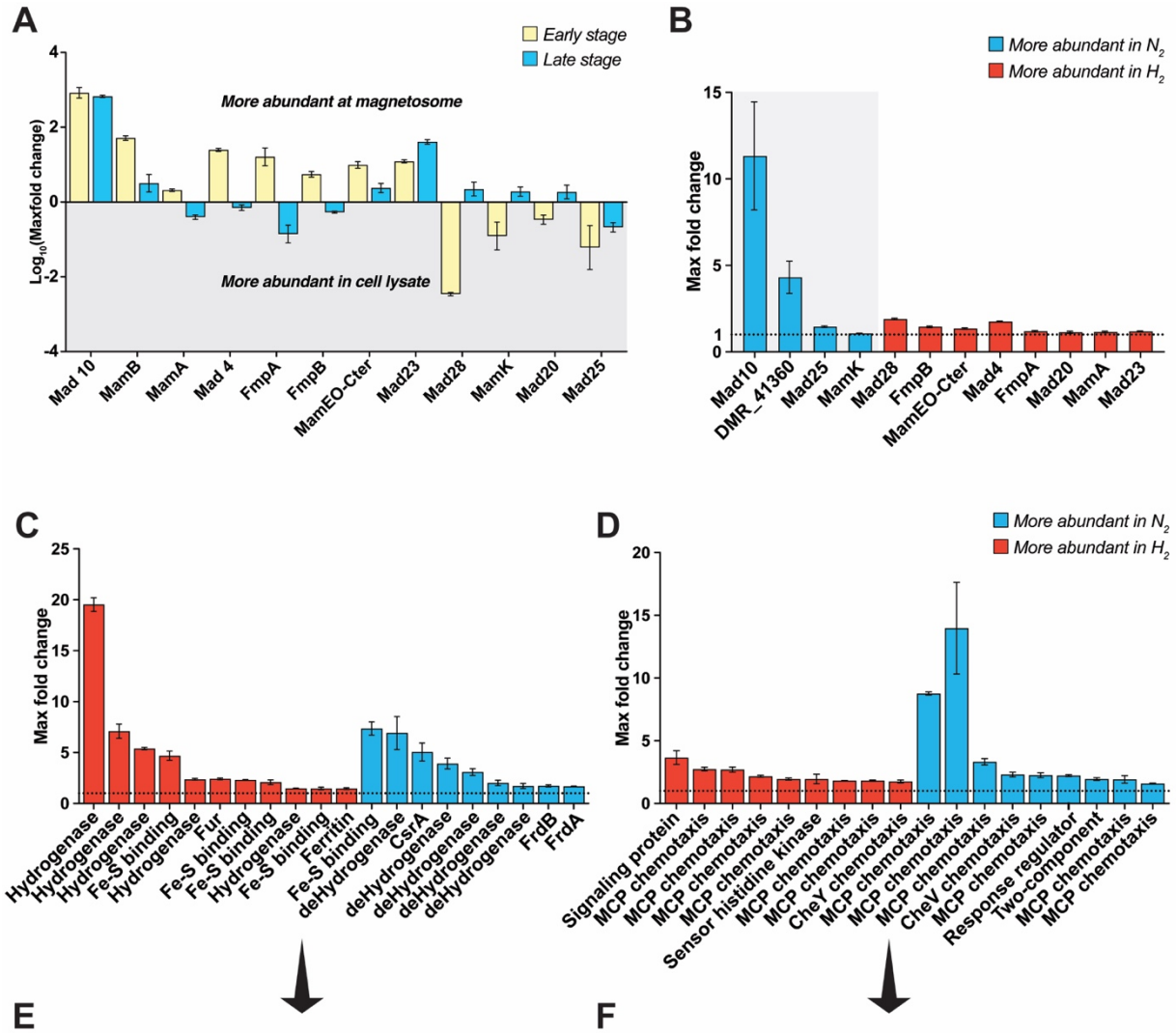

E

	Protein name	Highest
1	DMR_07840 Hydrogenase	Hydrogen
2	DMR_07830 Hydrogenase	Hydrogen
3	DMR_07850 Hydrogenase	Hydrogen
4	DMR_19790 Fur ferric uptake regulation	Hydrogen
5	DMR_01950 iron-sulfur binding	Hydrogen
6	DMR_01930 Hydrogenase	Hydrogen
7	DMR_01940 iron-sulfur binding	Hydrogen
8	DMR_20050 iron-sulfur binding	Hydrogen
9	DMR_12950 Hydrogenase	Hydrogen
10	DMR_17620 ferritin	Hydrogen
11	DMR_42710 iron-sulfur binding	Hydrogen
12	DMR_31480 csrA carbon storage regulator	Nitrogen
13	DMR_42500 iron-sulfur binding	Nitrogen
14	DMR_01890 deHydrogenase	Nitrogen
15	DMR_16050 deHydrogenase	Nitrogen
16	DMR_21490 deHydrogenase	Nitrogen
17	DMR_05780 frdB fumarate reductase	Nitrogen
18	DMR_19380 deHydrogenase	Nitrogen
19	DMR_08200 deHydrogenase	Nitrogen
20	DMR_34280 frdA fumarate reductase	Nitrogen

F

	Protein name	Highest
1	DMR_09360 signaling protein	Hydrogen
2	DMR_28950 methyl-accepting chemotaxis	Hydrogen
3	DMR_00340 methyl-accepting chemotaxis	Hydrogen
4	DMR_37860 methyl-accepting chemotaxis	Hydrogen
5	DMR_27200 methyl-accepting chemotaxis	Hydrogen
6	DMR_34160 sensor histidine kinase	Hydrogen
7	DMR_38310 methyl-accepting chemotaxis	Hydrogen
8	DMR_04320 methyl-accepting chemotaxis	Hydrogen
9	DMR_23920 CheY chemotaxis	Hydrogen
10	DMR_26500 methyl-accepting chemotaxis	Nitrogen
11	DMR_07950 methyl-accepting chemotaxis	Nitrogen
12	DMR_29030 methyl-accepting chemotaxis	Nitrogen
13	DMR_26640 CheV chemotaxis	Nitrogen
14	DMR_07730 methyl-accepting chemotaxis	Nitrogen
15	DMR_41540 response regulator	Nitrogen
16	DMR_45100 2-component sensor & regulator	Nitrogen
17	DMR_08750 methyl-accepting chemotaxis	Nitrogen
18	DMR_27400 methyl-accepting chemotaxis	Nitrogen

Supplemental S8. *Additional proteomics data.*

(A) Additional proteomic analysis of magnetosome proteins comparing protein abundance in the cell lysate versus the magnetosome fraction. The abundance of magnetosome proteins is

851 represented as greater than 1 when they are more prevalent in the magnetosome fraction and
852 as less than 1 when they are more abundant in the cell lysate. (B) The maximum fold change of
853 magnetosome proteins detected in cell lysates under both nitrogen and hydrogen conditions.
854 Blue bars represent proteins more abundant in nitrogen condition and orange bars represent
855 proteins more abundant in hydrogen condition. (C) and (D) Additional proteomic data comparing
856 protein abundance in nitrogen versus hydrogen conditions, highlighting non-magnetosome
857 proteins with significant maximum fold changes. (E) and (F) display the gene names and locus
858 IDs corresponding to all bars in (C) and (D), respectively.
859

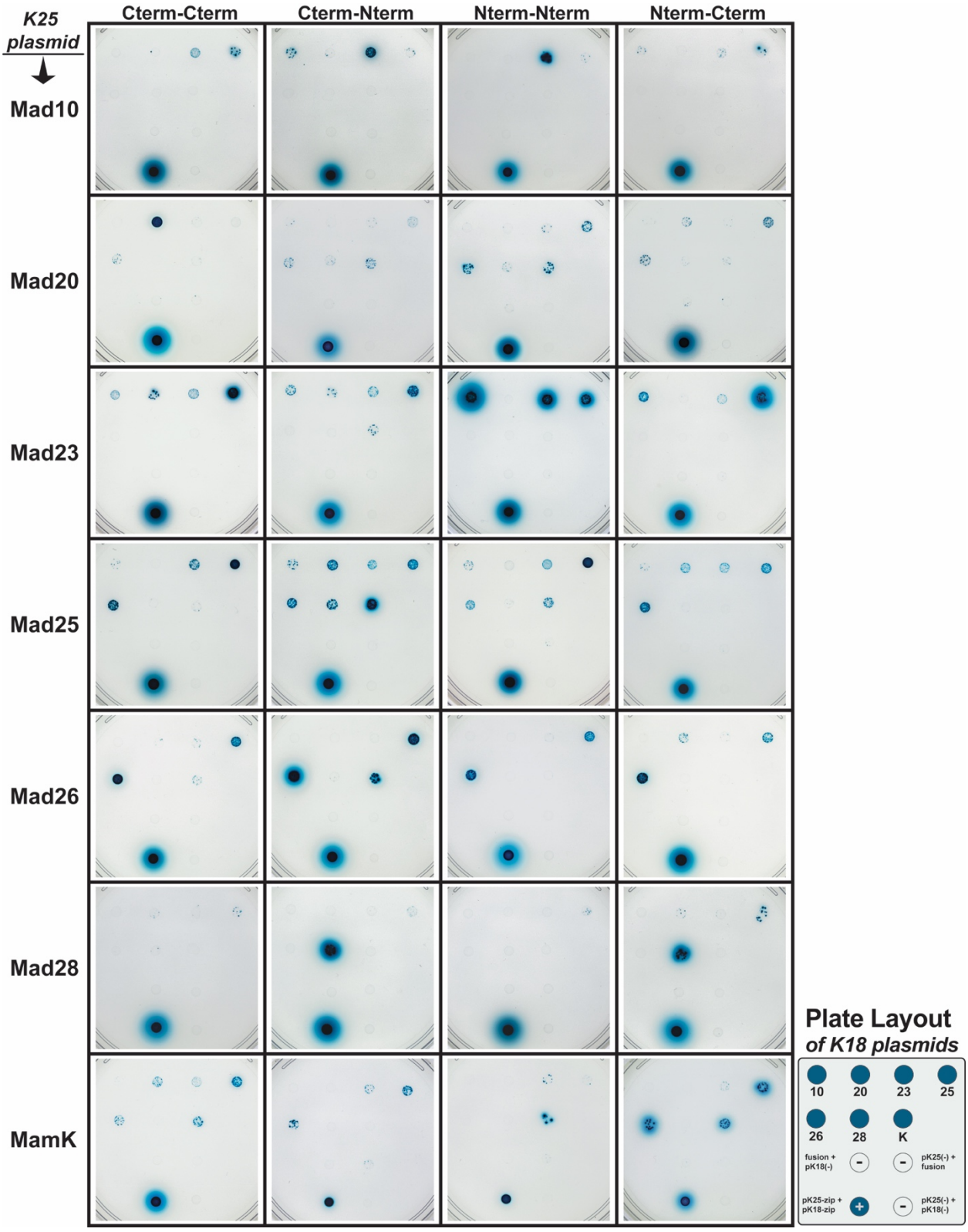

Supplemental S9. *BACTH images of plates for all interactions.*

862 Image of all plates used to construct the table of all of the interactions in Supplemental Figure
863 S2. The illustration on the bottom right shows the layout for each plate which included for
864 controls:
865
866 **Extended data Table:**
867

Phyla	Organiam	16S gene ID	Genome ID	Shape reference	MGC reference
Alpha	*Magnetospirillum magneticum* AMB-1	D17514.1	NCBI:txid342108	11	12
Alpha	*Magnetospirillum magnetotacticum* MS-1	IMG: 2647169949	NCBI:txid272627	13	14
Alpha	*Magnetospirillum caucaseum* SO-1	JX502622.2	NCBI:txid1244869	15	15–17
Alpha	*Magnetospirillum* ME-1	IMG: 2676550241	NCBI:txid1639348	18	16,17,19
Alpha	*Magnetospirillum* XM-1	KP966105.1	NCBI:txid1663591	20	16,21
Alpha	*Magnetospirillum marisnigri* SP-1	KC252630.3	NCBI:txid1285242	15	17,22
Alpha	*Magnetospirillum kuznetsovii* LBB-42	NR_180134.1	NCBI:txid2053833	23	16,23
Alpha	*Magnetospirillum gryphiswaldense* MSR-1	NR_121771.1	NCBI:txid431944	24,25	26
Alpha	*Magnetospirillum moscoviense* BB-1	KF712468.2	NCBI:txid1437059	15	17,22
Alpha	*Magnetospirillum* sp. LM-5	IMG: 2894467686	NCBI:txid2681466	27	17
Alpha	*Magnetospirillum* sp. SS-4	IMG: 2894461381	NCBI:txid2681465	27	17
Alpha	*Magnetospirillum* sp. UT-4	IMG: 2894472958	NCBI:txid2681467	27	17

Alpha	*Rhodospirillaceae* LM-1	JF490044.1	NCBI:txid1008128	27	17
Alpha	*Magnetospira* QH-2	EU675666.1	NCBI:txid1288970	28	29
Alpha	*Ca. Terasakiella magnetica* PR1	IMG: 2752957094	NCBI:txid1867952	30	30
Alpha	*Magnetovibrio blakemorei* MV-1	L06455.1	NCBI:txid28181	31	32
Gamma	Strain BW-2	HQ595728.1	NCBI:txid947515	33	34
Gamma	SHHR-1	KX344069.1	NCBI:txid1899433	35	16
Gamma	Strain SS-5	HQ595729.1	NCBI:txid947516	33	36
Eta	*Ca. Magnetococcus massalia* MO-1	EF643520.2	NCBI:txid451514	37	38
Eta	*Magnetococcus* MC-1	IMG: 640720050	NCBI:txid156889	39	40
Eta	*Magnetofaba australis* IT-1	JX534168.1	NCBI:txid1434232	41	41
Eta	*Ca. Magnetaquicoccus inordinatus* UR-1	IMG: 2881921666	NCBI:txid2496818	42	42
Desulfo-bacterota	*Ca. Magnetoglobus multicellularis*	IMG: 2559591426	NCBI:txid890399	43,44	45
Desulfo-bacterota	*Ca. Magnetananas rongchenensis* RPA	KF925363.1	NCBI:txid1463558	46	46
Desulfo-bacterota	*Ca. Magnetomorum* HK-1	IMG: 2648890082	NCBI:txid1509431	47	48
Desulfo-bacterota	*Desulfamplus magnetovallimortis* BW-1	JN252194.1	NCBI:txid1073250	49	50
Desulfo-bacterota	*Desulfovibrio magneticus* RS-1	NR_074958.1	NCBI:txid573370	51,52	53

Desulfo-bacterota	*Desulfovibrio* FSS-1	LC311577.1	NCBI:txid2730080	54	54
Desulfo-bacterota	*Delta Proteobacterium* FH-1	JF330268	NCBI:txid999117	50	50
Desulfo-bacterota	*Desulfonatronum* ML-1	HQ595725.1	NCBI:txid947513	55	50
Nitro-spirota	*Ca. Magnetoovum chiemensis* WYHC-5	OL423397.1	NCBI:txid1609970	56	56
Nitro-spirota	*Ca. Magnetobacterium casensis* MYR-1	MT703955.1	NCBI:txid1455061	57	58
Nitro-spirota	*Ca. Magnetobacterium bavaricum* TM-1	X71838.1	NCBI:txid29290	59	60
Nitro-spirota	*Ca. Nitrospirae* YQR-1	ON340538.1		16	16
Nitro-spirota	*Ca. Magnetomonas plexicatena* LBB-01	MK632185.1	CP049016.1	61	61
Nitro-spirota	*Ca. Magnetominusculus linsii* LBB-02	MK632186.1		61	61
Nitro-spirota	*Ca. Nitrospirae* MYC-10	ON342894.1		16	16
Nitro-spirota	*Ca. Magnetocorallium paracelense* XS-1	OQ281288.1	NCBI:txid3021403	62	62
Elusi-microbiota	*Ca. Liberimonas magnetica DUR002*	KY516811	GCA_020523885.1	5	5
Elusi-microbiota	*Ca. Obscuribacterium magneticum DUR003*	JQ369221	GCA_020523905.1	5	5
OP3	*Ca. Omnitrophus magneticus* SKK-01	JN412733.1	NCBI:txid174292	63	60

Supplemental Table 1. *Table of species and reference used for phylogenetic tree construction*

871 **Supplemental Tables**

872

Strain	Description	Reference
AK80	WT	[64]
AK268	WT, Δ*upp*	[65]
AK350	Δ*mad23*, Δ*upp*	This study
AK377	Δ*mad20*, Δ*upp*	This study
AK378	Δ*mad25*, Δ*upp*	This study
AK380	Δ*mad10*, Δ*upp*	This study
AK382	Δ*mad28*, Δ*upp*	This study
AK383	Δ*mad26*, Δ*upp*	This study
AK220	Δ*mamK*	This study

873 **Supplemental Table 2.** *Table of all strains used in this study*

874

Plasmid	Description	Backbone	Reference
PAK906	Complementation backbone with pNTP		[64]
PAK907	Complementation backbone with pmamA		[64]
pAK914	Deletion backbone with SacB only		[64]
pAK1127	Deletion backbone with Upp and SacB		[65]
pAK1452	mad10 deletion plasmid with Strep	pAK1127	This study
pAK1384	mad20 deletion plasmid with StrAB	pAK1127	This study
pAK1268	mad23 deletion with strAB for selection and upp counterselection (pCG116)	pAK1127	This study
pAK1386	mad25 deletion plasmid with StrAB	pAK1127	This study
pAK1387	mad26 deletion plasmid with StrAB	pAK1127	This study
pAK1388	mad28 deletion plasmid with StrAB	pAK1127	This study
pAK966	mamK deletion plasmid with strAB in pAK914	pAK914	This study
pAK1481	pAK906–mad10 Complementation	pAK906	This study
pAK1454	pAK906–mad20 complementation	pAK906	This study
pAK1507	pAK906–mad23 complementation	pAK906	This study
pAK1480	pAK907–mad25 Complementation	pAK907	This study
pAK1488	pAK907–mad26 Complementation	pAK907	This study

pAK1518	pAK907– mad28 Complementation (with alt Start)	pAK907	This study
pAK1489	pAK906–mamK Complementation	pAK906	This study
pAK318	pKT25		EUROMEDEX
pAK319	pKNT25		EUROMEDEX
pAK320	pUT18		EUROMEDEX
pAK321	pUT18C		EUROMEDEX
pAK322	pKT25-zip		EUROMEDEX
pAK323	pUT18C-zip		EUROMEDEX
pAK1525	KT25-mad10	pAK318	This study
pAK1526	mad10-KNT25	pAK319	This study
pAK1527	mad10-UT18	pAK320	This study
pAK1528	UT18C-mad10	pAK321	This study
pAK1529	KT25-mad20	pAK318	This study
pAK1530	mad20-KNT25	pAK319	This study
pAK1531	mad20-UT18	pAK320	This study
pAK1532	UT18C-mad20	pAK321	This study
pAK1541	KT25-mad23	pAK318	This study
pAK1542	mad23-KNT25	pAK319	This study
pAK1543	mad23-UT18	pAK320	This study
pAK1544	UT18C-mad23	pAK321	This study
pAK1549	KT25-mad25	pAK318	This study
pAK1550	mad25-KNT25	pAK319	This study
pAK1551	mad25-UT18	pAK320	This study
pAK1552	UT18C-mad25	pAK321	This study
pAK1553	KT25-mad26	pAK318	This study
pAK1554	mad26-KNT25	pAK319	This study
pAK1555	mad26-UT18	pAK320	This study
pAK1556	UT18C-mad26	pAK321	This study
pAK1557	KT25-mad28	pAK318	This study
pAK1558	mad28-KNT25	pAK319	This study
pAK1559	mad28-UT18	pAK320	This study
pAK1560	UT18C-mad28	pAK321	This study

pAK1561	KT25-mamK	pAK318	This study
pAK1562	mamK-KNT25	pAK319	This study
pAK1563	mamK-UT18	pAK320	This study
pAK1564	UT18C-mamK	pAK321	This study

875 **Supplemental Table 3.** *Table of all plasmids used in this study*

876 All of the plasmids used for this study and the previously published backbones used to generate
877 the plasmids used for this research.

878

Primer	Sequence	Description
VR123-F	AAACGCAAAAGAAAATGCCGATATCCTATTG GCCTCTAGAGGAATTCCAGGATTCCCTCA	mad20 deletion upstream
VR124-R	GGATCCCCCATCCACTAAATTTAAATAGGATC CTCTGTCCTTAATCTTGGCC	mad20 deletion upstream
VR125-F	GGATCCTATTTAAATTTAGTGGATGGGGGAT CCAGGATCGCCAACAATGCCTG	mad20 deletion downstream
VR126-R	TGGCGGTCATGGTCTTTTCGGCGAGCTTCTC TAGAAGCTCCGCTTCAAGAACCAC	mad20 deletion downstream
VR127-F	AAACGCAAAAGAAAATGCCGATATCCTATTG GCCTCTAGACAAGTGGAGTTAGGGTGATT	mad25 deletion upstream
VR128-R	CATATGCCCATCCACTAAATTTAAATACATAT GGTCAGCTTTAAAAAGGGCCA	mad25 deletion upstream
VR129-F	CATATGTATTTAAATTTAGTGGATGGGCATAT GTGTTCGGCCATTGCCGTTAT	mad25 deletion downstream
VR130-R	TGGTGGCGGTCATGGTCTTTTCGGCGAGCTT CTCTAGACCTCGTCTCTCTAACACAAA	mad25 deletion downstream
VR131-F	AAACGCAAAAGAAAATGCCGATATCCTATTG GCCTCTAGACATCAAAAGCATGGAAGGGC	mad26 deletion upstream
VR132-R	GGATCCCCCATCCACTAAATTTAAATAGGATC CTTCGCGCTGCATTCCGTCCA	mad26 deletion upstream
VR133-F	GGATCCTATTTAAATTTAGTGGATGGGGGAT CCACTATTGCCTTGAATAAATG	mad26 deletion downstream
VR134-R	TGGTGGCGGTCATGGTCTTTTCGGCGAGCTT CTCTAGAGCATCCAAGCGTTCTTTTTG	mad26 deletion downstream

VR135-F	AAACGCAAAAGAAAATGCCGATATCCTATTGGCCTCTAGAAACGGTTTACAGCGGATACA	mad28 deletion upstream
VR136-R	GGATCCCCCATCCACTAAATTTAAATAGGATCCGCATCCAAGCGTTCTTTTTG	mad28 deletion upstream
VR137-F	GGATCCTATTTAAATTTAGTGGATGGGGGATCCGGCCCTGACCGAGGCGGATT	mad28 deletion downstream
VR138-R	TGGCGGTCATGGTCTTTTCGGCGAGCTTCTCTAGACAAAATGGAGATTGGAGGAA	mad28 deletion downstream
VR147-F	AGGCGGGCATGGCCAAGATTAAGGACAGAGGATCCCTGCTAAAGGAAGCGGAACACG	Add StrAB-mad20-F
VR148-R	ATTCGCTATCAGGCATTGTTGGCGATCCTGGATCCCTAGTATGACGTCTGTCGCACCT	Add StrAB-mad20-R
VR149-F	AGGGGCCATGGCCCTTTTTAAAGCTGACCATATGCTGCTAAAGGAAGCGGAACACG	Add StrAB-mad25-F
VR150-R	GAAAAAGCATAACGGCAATGGCCGAACACATATGCTAGTATGACGTCTGTCGCACCT	Add StrAB-mad25-R
VR151-F	GGGCAAACACTCCCGGTCGATTCCGGACAGGATCCCTGCTAAAGGAAGCGGAACACG	Add StrAB-mad26-F
VR152-R	ATCACAGTTCATTTATTCAAGGCAATAGTGGATCCCTAGTATGACGTCTGTCGCACCT	Add StrAB-mad26-R
VR153-F	ATATTCGAGCAAAAAGAACGCTTGGATGCGGATCCCTGCTAAAGGAAGCGGAACACG	Add StrAB-mad28-F
VR154-R	GGTATGGCTAATCCGCCTCGGTCAGGGCCGGATCCCTAGTATGACGTCTGTCGCACCT	Add StrAB-mad28-R
VR319-F	GTCATGGTCTTTTCGGCGAGCTTCTCTAGAATCTCCAAAAAGTTGCTGGGC	mad10 deletion upstream
VR320-R	CCCATCCACTAAATTTAAATAGGATCCTCTTCCATGGCGTCCTCCG	mad10 deletion upstream
VR321-F	TATTTAAATTTAGTGGATGGGGGATCCCCAGTGCGCAGCCGGCCTGA	mad10 deletion downstream
VR322-R	GAAAATGCCGATATCCTATTGGCCTCTAGATCGCGGCCTGGGCC	mad10 deletion downstream

VR323-F	CGACAATGCGCGGAGGACGCCATGGAAGAGCTGCTAAAGGAAGCGGAACAC	Add StrAB-mad10-F
VR324-R	GAGATGATCTCAGGCCGGCTGCGCACTGGGCTAGTATGACGTCTGTCGCACC	Add StrAB-mad10-R
VR277-F	AGACAGGATGAGGATCGTTTCGCGTCGACTGATCATCTCCCGGCGGG	mad20 complementation in pAK906
VR278-R	GGGAATTCGAGCTCGGTACCCGGGGATCCTGCGCCGCTCCTGGATTC	mad20 complementation in pAK906
CG220-R	GAGCTCGGTACCCGGGGATCCTCTAGAACTTGCTTTTCCGCCGTCATAC	mad23 complementation in pAK906
CG221-F	CAAGAGACAGGATGAGGATCGTTTCGCGATGGAAGACGCCATGAGCTC	mad23 complementation in pAK906
VR335-F	AAGCCAAGAAAAACGTCGCCAACGTCGACTATGGCCCTTTTTAAAGCTGACG	mad25 complementation in pAK907
VR336-R	GGGAATTCGAGCTCGGTACCCGGGGATCCTCTACCCGTCTGCGACGTC	mad25 complementation in pAK907
VR337-F	AGACAGGATGAGGATCGTTTCGCGTCGACTATGGAAGAAAATACCCGCTACA	mad10 complementation in pAK906
VR338R	GGGAATTCGAGCTCGGTACCCGGGGATCCTTCAGGCCGGCTGCG	mad10 complementation in pAK906
VR355-F	AAGCCAAGAAAAACGTCGCCAACGTCGACTATGGACGGAATGCAGCGC	mad26 complementation in pAK907

VR356-R	GGGAATTCGAGCTCGGTACCCGGGGATCCTTCATTTATTCAAGGCAATAGTCAGT	mad26 complementation in pAK907
VR357-F	AGACAGGATGAGGATCGTTTCGCGTCGACTATGTCCGGAAGCAACGTGC	mamK complementation in pAK906
VR358-R	GGGAATTCGAGCTCGGTACCCGGGGATCCTTTAATCCTTTCGCAGCTCGTC	mamK complementation in pAK906
VR375-F	AAGCCAAGAAAAACGTCGCCAACGTCGACTACAGCTCTGGCGCTCTTG	mad28 complementation in pAK907 (with pmad28 & alt-start)
VR372-R	GGGAATTCGAGCTCGGTACCCGGGGATCCTCTAATCCGCCTCGGTCAGG	mad28 complementation in pAK907 (with pmad28 & alt-start)
VR390-F	CGGGCTGCAGGGTCGACTCTAGAGGATCCCATGGAAGAAAATACCCGCTACA	KT25_mad10
VR391-R	TCACGACGTTGTAAAACGACGGCCGAATTCTCAGGCCGGCTGCG	KT25_mad10
VR392-F	ACAGCTATGACCATGATTACGCCAAGCTTGATGGAAGAAAATACCCGCTACA	KNT25_mad10-noStop
VR393-R	CCGGGGATCCTCTAGAGTCGACCTGCAGGCGGCCGGCTGCGCA	KNT25_mad10-noStop
VR394-F	ACAGCTATGACCATGATTACGCCAAGCTTGATGGAAGAAAATACCCGCTACA	UT18_mad10-NoStop
VR395-R	CCGGGGATCCTCTAGAGTCGACCTGCAGGCGGCCGGCTGCGCA	UT18_mad10-NoStop
VR396-F	CGCCACTGCAGGTCGACTCTAGAGGATCCCATGGAAGAAAATACCCGCTACA	UT18C_mad10
VR397-R	TAGTTATATCGATGAATTCGAGCTCGGTACTCAGGCCGGCTGCG	UT18C_mad10
VR398-F	CGGGCTGCAGGGTCGACTCTAGAGGATCCCATGGCCAAGATTAAGGACAGACT	KT25_mad20

VR399-R	TCACGACGTTGTAAAACGACGGCCGAATTCTCAGGCATTGTTGGCGATCC	KT25_mad20
VR400-F	ACAGCTATGACCATGATTACGCCAAGCTTGATGGCCAAGATTAAGGACAGACT	KNT25_mad20-noStop
VR401-R	CCGGGGATCCTCTAGAGTCGACCTGCAGGCGGCATTGTTGGCGATCCTCT	KNT25_mad20-noStop
VR402-F	ACAGCTATGACCATGATTACGCCAAGCTTGATGGCCAAGATTAAGGACAGACT	UT18_mad20-NoStop
VR403-R	CCGGGGATCCTCTAGAGTCGACCTGCAGGCGGCATTGTTGGCGATCCTCT	UT18_mad20-NoStop
VR404-F	CGCCACTGCAGGTCGACTCTAGAGGATCCCATGGCCAAGATTAAGGACAGACT	UT18C_mad20
VR405-R	TAGTTATATCGATGAATTCGAGCTCGGTACTCAGGCATTGTTGGCGATCC	UT18C_mad20
VR422-F	CGGGCTGCAGGGTCGACTCTAGAGGATCCCATGGAAGACGCCATGAGCTC	KT25_mad23
VR423-R	TCACGACGTTGTAAAACGACGGCCGAATTCCTAACTCCACTTGTAGCGCA	KT25_mad23
VR424-F	ACAGCTATGACCATGATTACGCCAAGCTTGATGGAAGACGCCATGAGCTC	KNT25_mad23-noStop
VR425-R	CCGGGGATCCTCTAGAGTCGACCTGCAGGCACTCCACTTGTAGCGCATGC	KNT25_mad23-noStop
VR426-F	ACAGCTATGACCATGATTACGCCAAGCTTGATGGAAGACGCCATGAGCTC	UT18_mad23-NoStop
VR427-R	CCGGGGATCCTCTAGAGTCGACCTGCAGGCACTCCACTTGTAGCGCATGC	UT18_mad23-NoStop
VR428-F	CGCCACTGCAGGTCGACTCTAGAGGATCCCATGGAAGACGCCATGAGCTC	UT18C_mad23
VR429-R	TAGTTATATCGATGAATTCGAGCTCGGTACCTAACTCCACTTGTAGCGCA	UT18C_mad23
VR438-F	CGGGCTGCAGGGTCGACTCTAGAGGATCCCATGGCCCTTTTTAAAGCTGACG	KT25_mad25

VR439-R	TCACGACGTTGTAAAACGACGGCCGAATTCC TACCCGTCTGCGACGTC	KT25_mad25
VR440-F	ACAGCTATGACCATGATTACGCCAAGCTTGA TGGCCCTTTTTAAAGCTGACG	KNT25_mad25-noStop
VR441-R	CCGGGGATCCTCTAGAGTCGACCTGCAGGC CCCGTCTGCGACGTCG	KNT25_mad25-noStop
VR442-F	ACAGCTATGACCATGATTACGCCAAGCTTGA TGGCCCTTTTTAAAGCTGACG	UT18_mad25-NoStop
VR443-R	CCGGGGATCCTCTAGAGTCGACCTGCAGGC CCCGTCTGCGACGTCG	UT18_mad25-NoStop
VR444-F	CGCCACTGCAGGTCGACTCTAGAGGATCCCA TGGCCCTTTTTAAAGCTGACG	UT18C_mad25
VR445-R	TAGTTATATCGATGAATTCGAGCTCGGTACCT ACCCGTCTGCGACGTC	UT18C_mad25
VR446-F	CGGGCTGCAGGGTCGACTCTAGAGGATCCC ATGGACGGAATGCAGCGC	KT25_mad26
VR447-R	TCACGACGTTGTAAAACGACGGCCGAATTCT CATTTATTCAAGGCAATAGTCAGT	KT25_mad26
VR448-F	ACAGCTATGACCATGATTACGCCAAGCTTGA TGGACGGAATGCAGCGC	KNT25_mad26-noStop
VR449-R	CCGGGGATCCTCTAGAGTCGACCTGCAGGC TTTATTCAAGGCAATAGTCAGTTCA	KNT25_mad26-noStop
VR450-F	ACAGCTATGACCATGATTACGCCAAGCTTGA TGGACGGAATGCAGCGC	UT18_mad26-NoStop
VR451-R	CCGGGGATCCTCTAGAGTCGACCTGCAGGC TTTATTCAAGGCAATAGTCAGTTCA	UT18_mad26-NoStop
VR452-F	CGCCACTGCAGGTCGACTCTAGAGGATCCCA TGGACGGAATGCAGCGC	UT18C_mad26
VR453-R	TAGTTATATCGATGAATTCGAGCTCGGTACTC ATTTATTCAAGGCAATAGTCAGT	UT18C_mad26
VR454-F	CGGGCTGCAGGGTCGACTCTAGAGGATCCC ATGTCCCAAGAGGATAAGGCG	KT25_mad28

VR455-R	TCACGACGTTGTAAAACGACGGCCGAATTCCTAATCCGCCTCGGTCAGG	KT25_mad28
VR456-F	ACAGCTATGACCATGATTACGCCAAGCTTGATGTCCCAAGAGGATAAGGCG	KNT25_mad28-noStop
VR457-R	CCGGGGATCCTCTAGAGTCGACCTGCAGGCATCCGCCTCGGTCAGGG	KNT25_mad28-noStop
VR458-F	ACAGCTATGACCATGATTACGCCAAGCTTGATGTCCCAAGAGGATAAGGCG	UT18_mad28-NoStop
VR459-R	CCGGGGATCCTCTAGAGTCGACCTGCAGGCATCCGCCTCGGTCAGGG	UT18_mad28-NoStop
VR460-F	CGCCACTGCAGGTCGACTCTAGAGGATCCCATGTCCCAAGAGGATAAGGCG	UT18C_mad28
VR461-R	TAGTTATATCGATGAATTCGAGCTCGGTACCTAATCCGCCTCGGTCAGG	UT18C_mad28
VR462-F	CGGGCTGCAGGGTCGACTCTAGAGGATCCCATGTCCGGAAGCAACGTGC	KT25_mamK
VR463-R	TCACGACGTTGTAAAACGACGGCCGAATTCTTAATCCTTTCGCAGCTCGTC	KT25_mamK
VR464-F	ACAGCTATGACCATGATTACGCCAAGCTTGATGTCCGGAAGCAACGTGC	KNT25_mamK-noStop
VR465-R	CCGGGGATCCTCTAGAGTCGACCTGCAGGCATCCTTTCGCAGCTCGTCC	KNT25_mamK-noStop
VR466-F	ACAGCTATGACCATGATTACGCCAAGCTTGATGTCCGGAAGCAACGTGC	UT18_mamK-NoStop
VR467-R	CCGGGGATCCTCTAGAGTCGACCTGCAGGCATCCTTTCGCAGCTCGTCC	UT18_mamK-NoStop
VR468-F	CGCCACTGCAGGTCGACTCTAGAGGATCCCATGTCCGGAAGCAACGTGC	UT18C_mamK
VR469-R	TAGTTATATCGATGAATTCGAGCTCGGTACTTAATCCTTTCGCAGCTCGTC	UT18C_mamK

Supplemental Table 4. *Table of all primers used in this study*

		Compared with:	Mann-Whitney U test		Welch's T-Test	
Figure	**Strain/ Condition**	**Strain/ Condition**	**pValue**	**Significance**	**pValue**	**Significance**
Figure 3C	Early	Late	<0.0001	****	<0.0001	****
Figure 3D	Early	Late	<0.0001	****	<0.0001	****
Figure 3E	Early	Late	<0.0001	****	<0.0001	****
Figure 3I	Immature crystals	Mature crystals	---	---	0.0006	***

881 **Supplemental Table 5.** *Table of all statistical tests used for figure 3 in this study*

882

		Compared with:	One way ANOVA test		Mann-Whitney U test	
Figure	**Strain/ Condition**	**Strain/ Condition**	**pValue**	**Significance**	**pValue**	**Significance**
Figure 4D	*fmpA*	WT	<0.0001	****	<0.0001	****
Figure 4D	*fmpB*	WT	<0.0001	****	<0.0001	****
Figure 4E	*fmpA*	WT	<0.0001	****	<0.0001	****
Figure 4E	*fmpB*	WT	<0.0001	****	<0.0001	****
Figure 4F	*fmpA*	WT	<0.0001	****	<0.0001	****
Figure 4F	*fmpB*	WT	<0.0001	****	<0.0001	****

883 **Supplemental Table 6.** *Table of all statistical tests used for Figure 4 in this study*

884

		Compared with:	One way ANOVA test		Mann-Whitney U test	
Figure	**Strain/ Condition**	**Strain/ Condition**	**pValue**	**Significance**	**pValue**	**Significance**
Figure 5N*i*	Δ*mamK*	WT	<0.0001	****	<0.0001	****
Figure 5N*i*	Δ*mad28*	WT	0.9378	ns	0.4697	ns
Figure 5N*ii*	Δ*mamK*	WT	<0.0001	****	<0.0001	****

Figure 5N*ii*	Δ*mad28*	WT	0.0703	ns	0.0053	**

885 **Supplemental Table 7.** *Table of all statistical tests used for figure 5 in this study*

886

887

		Compared with:	One way ANOVA test		Mann-Whitney U test	
Supplemental Figure	**Strain/ Condition**	**Strain/ Condition**	**pValue**	**Significance**	**pValue**	**Significance**
Figure S1D	Δ*mad10*	WT	0.1364	ns	0.0005	***
Figure S1D	Δ*mad20*	WT	0.7606	ns	0.3754	ns
Figure S1D	Δ*mad23*	WT	0.7606	ns	0.5328	ns
Figure S1D	Δ*mad25*	WT	0.3521	ns	0.0147	*
Figure S1D	Δ*mad26*	WT	0.4881	ns	0.111	ns
Figure S1D	Δ*mad28*	WT	0.7606	ns	0.3365	ns
Figure S1D	Δ*mamK*	WT	<0.0001	****	<0.0001	****

888

		Compared with:	One way ANOVA test	
Supplemental Figure	**Strain/Condition**	**Strain/Condition**	**pValue**	**Significance**
Figure S1E	Δ*mad10*	WT	<0.0001	****
Figure S1E	Δ*mad20*	WT	0.0001	***
Figure S1E	Δ*mad23*	WT	0.5127	ns
Figure S1E	Δ*mad25*	WT	0.9895	ns
Figure S1E	Δ*mad26*	WT	0.0953	ns
Figure S1E	Δ*mad28*	WT	0.0381	*
Figure S1E	Δ*mamK*	WT	<0.0001	****

889

		Compared with:	Kruskal-Wallis test	
Supplemental Figure	**Strain/Condition**	**Strain/Condition**	**pValue**	**Significance**
Figure S1F	Δ*mad10*	WT	<0.0001	****
Figure S1F	Δ*mad20*	WT	<0.0001	****
Figure S1F	Δ*mad23*	WT	0.2744	ns

Figure S1F	Δ*mad25*	WT	0.0073	**
Figure S1F	Δ*mad26*	WT	0.0805	ns
Figure S1F	Δ*mad28*	WT	0.0007	***
Figure S1F	Δ*mamK*	WT	<0.0001	****

890 **Supplemental Table 8.** *Tables of all statistical tests used for Supplemental Figure S1 in this*
891 *study*
892

References:

1. Liu, Y., Van Den Ent, F. & Löwe, J. Filament structure and subcellular organization of the bacterial intermediate filament–like protein crescentin. *Proc. Natl. Acad. Sci. U.S.A.* **121**, e2309984121 (2024).
2. Pohl, A. *et al.* Decoding Biomineralization: Interaction of a Mad10-Derived Peptide with Magnetite Thin Films. *Nano Lett.* **19**, 8207–8215 (2019).
3. Paysan-Lafosse, T. *et al.* InterPro in 2022. *Nucleic Acids Research* **51**, D418–D427 (2023).
4. Kearse, M. *et al.* Geneious Basic: An integrated and extendable desktop software platform for the organization and analysis of sequence data. *Bioinformatics* **28**, 1647–1649 (2012).
5. Uzun, M. *et al.* Recovery and genome reconstruction of novel magnetotactic Elusimicrobiota from bog soil. *The ISME Journal* **17**, 204–214 (2023).
6. Gilchrist, C. L. M. & Chooi, Y.-H. clinker & clustermap.js: automatic generation of gene cluster comparison figures. *Bioinformatics* **37**, 2473–2475 (2021).
7. Hallgren, J. *et al.* DeepTMHMM predicts alpha and beta transmembrane proteins using deep neural networks. Preprint at https://doi.org/10.1101/2022.04.08.487609 (2022).
8. Ludwiczak, J., Winski, A., Szczepaniak, K., Alva, V. & Dunin-Horkawicz, S. DeepCoil—a fast and accurate prediction of coiled-coil domains in protein sequences. *Bioinformatics* **35**, 2790–2795 (2019).
9. Mirdita, M. *et al.* ColabFold: making protein folding accessible to all. *Nat Methods* **19**, 679–682 (2022).
10. Meng, E. C. *et al.* UCSF ChimeraX: Tools for structure building and analysis. *Protein Sci* **32**, e4792 (2023).
11. Li, J. & Pan, Y. Environmental Factors Affect Magnetite Magnetosome Synthesis in Magnetospirillum magneticum AMB-1: Implications for Biologically Controlled Mineralization. *Geomicrobiology Journal* **29**, 362–373 (2012).

922 12. Matsunaga, T. *et al.* Complete genome sequence of the facultative anaerobic
923 magnetotactic bacterium Magnetospirillum sp. strain AMB-1. *DNA Res* **12**, 157–166
924 (2005).
925 13. Maratea, D. & Blakemore, R. P. Aquaspirillum magnetotacticum sp. nov., a Magnetic
926 Spirillum. *International Journal of Systematic and Evolutionary Microbiology* **31**,
927 452–455 (1981).
928 14. Smalley, M. D., Marinov, G. K., Bertani, L. E. & DeSalvo, G. Genome Sequence of
929 Magnetospirillum magnetotacticum Strain MS-1. *Genome Announc* **3**, e00233-15
930 (2015).
931 15. Dziuba, M. *et al.* Magnetospirillum caucaseum sp. nov., Magnetospirillum marisnigri
932 sp. nov. and Magnetospirillum moscoviense sp. nov., freshwater magnetotactic
933 bacteria isolated from three distinct geographical locations in European Russia.
934 *International Journal of Systematic and Evolutionary Microbiology* **66**, 2069–2077
935 (2016).
936 16. Liu, P. *et al.* Key gene networks that control magnetosome biomineralization in
937 magnetotactic bacteria. *National Science Review* **10**, nwac238 (2023).
938 17. Monteil, C. L. *et al.* Repeated horizontal gene transfers triggered parallel evolution of
939 magnetotaxis in two evolutionary divergent lineages of magnetotactic bacteria. *The*
940 *ISME Journal* **14**, 1783–1794 (2020).
941 18. Ke, L. *et al.* Characteristics and optimised fermentation of a novel magnetotactic
942 bacterium, Magnetospirillum sp. ME-1. *FEMS Microbiology Letters* **365**, fny052
943 (2018).
944 19. Ke, L., Liu, P., Liu, S. & Gao, M. Complete Genome Sequence of Magnetospirillum
945 sp. ME-1, a Novel Magnetotactic Bacterium Isolated from East Lake, Wuhan, China.
946 *Genome Announc* **5**, e00485-17 (2017).
947 20. Wang, Y. *et al.* Characterizing and optimizing magnetosome production of
948 Magnetospirillum sp. XM-1 isolated from Xi'an City Moat, China. *FEMS Microbiology*
949 *Letters* **362**, fnv167 (2015).
950 21. Wang, Y. *et al.* Complete Genome Sequence of Magnetospirillum sp. Strain XM-1,
951 Isolated from the Xi'an City Moat, China. *Genome Announc* **4**, e01171-16 (2016).

952 22. Koziaeva, V. V. *et al.* Draft Genome Sequences of Two Magnetotactic Bacteria,
953 Magnetospirillum moscoviense BB-1 and Magnetospirillum marisnigri SP-1.
954 *Genome Announc* **4**, e00814-16 (2016).
955 23. Koziaeva, V. V. *et al.* Magnetospirillum kuznetsovii sp. nov., a novel magnetotactic
956 bacterium isolated from a lake in the Moscow region. *International Journal of*
957 *Systematic and Evolutionary Microbiology* **69**, 1953–1959 (2019).
958 24. Fdez-Gubieda, M. L. *et al.* Magnetite Biomineralization in Magnetospirillum
959 gryphiswaldense: Time-Resolved Magnetic and Structural Studies. *ACS Nano* **7**,
960 3297–3305 (2013).
961 25. Schleifer, K. H. *et al.* The Genus *Magnetospirillum* gen. nov. Description of
962 *Magnetospirillum gryphiswaldense* sp. nov. and Transfer of *Aquaspirillum*
963 *magnetotacticum* to *Magnetospirillum magnetotacticum* comb. nov. *Systematic and*
964 *Applied Microbiology* **14**, 379–385 (1991).
965 26. Wang, X. *et al.* Complete Genome Sequence of Magnetospirillum gryphiswaldense
966 MSR-1. *Genome Announc* **2**, e00171-14 (2014).
967 27. Lefèvre, C. T. *et al.* Insight into the Evolution of Magnetotaxis in Magnetospirillum
968 spp., Based on *mam* Gene Phylogeny. *Appl Environ Microbiol* **78**, 7238–7248
969 (2012).
970 28. Zhu, K. *et al.* Isolation and characterization of a marine magnetotactic spirillum
971 axenic culture QH-2 from an intertidal zone of the China Sea. *Research in*
972 *Microbiology* **161**, 276–283 (2010).
973 29. Ji, B. *et al.* Comparative genomic analysis provides insights into the evolution and
974 niche adaptation of marine Magnetospira sp. QH-2 strain. *Environmental*
975 *Microbiology* **16**, 525–544 (2014).
976 30. Monteil, C. L. *et al.* Genomic study of a novel magnetotactic Alphaproteobacteria
977 uncovers the multiple ancestry of magnetotaxis. *Environmental Microbiology* **20**,
978 4415–4430 (2018).
979 31. Bazylinski, D. A. *et al.* Magnetovibrio blakemorei gen. nov., sp. nov., a
980 magnetotactic bacterium (Alphaproteobacteria: Rhodospirillaceae) isolated from a
981 salt marsh. *International Journal of Systematic and Evolutionary Microbiology* **63**,
982 1824–1833 (2013).

983 32. Trubitsyn, D. *et al.* Draft Genome Sequence of Magnetovibrio blakemorei Strain MV-
984 1, a Marine Vibrioid Magnetotactic Bacterium. *Genome Announc* **4**, e01330-16
985 (2016).
986 33. Lefèvre, C. T. *et al.* Novel magnetite-producing magnetotactic bacteria belonging to
987 the Gammaproteobacteria. *ISME J* **6**, 440–450 (2012).
988 34. Geurink, C. *et al.* Complete Genome Sequence of Strain BW-2, a Magnetotactic
989 Gammaproteobacterium in the Family Ectothiorhodospiraceae, Isolated from a
990 Brackish Spring in Death Valley, California. *Microbiol Resour Announc* **9**, e01144-19
991 (2020).
992 35. Li, J. *et al.* Single-Cell Resolution of Uncultured Magnetotactic Bacteria via
993 Fluorescence-Coupled Electron Microscopy. *Appl Environ Microbiol* **83**, e00409-17
994 (2017).
995 36. Trubitsyn, D. *et al.* Complete Genome Sequence of Strain SS-5, a Magnetotactic
996 Gammaproteobacterium Isolated from the Salton Sea, a Shallow, Saline, Endorheic
997 Rift Lake Located on the San Andreas Fault in California. *Microbiol Resour Announc*
998 **10**, e00928-20 (2021).
999 37. Lefèvre, C. T., Bernadac, A., Yu-Zhang, K., Pradel, N. & Wu, L.-F. Isolation and
1000 characterization of a magnetotactic bacterial culture from the Mediterranean Sea.
1001 *Environmental Microbiology* **11**, 1646–1657 (2009).
1002 38. Ji, B. *et al.* The chimeric nature of the genomes of marine magnetotactic coccoid-
1003 ovoid bacteria defines a novel group of Proteobacteria. *Environmental Microbiology*
1004 **19**, 1103–1119 (2017).
1005 39. Meldrum, F. C., Mann, S., Heywood, B. R., Frankel, R. B. & Bazylinski, D. A.
1006 Electron microscopy study of magnetosomes in a cultured coccoid magnetotactic
1007 bacterium. *Proceedings of the Royal Society of London. Series B: Biological*
1008 *Sciences* **251**, 231–236 (1993).
1009 40. Schübbe, S. *et al.* Complete Genome Sequence of the Chemolithoautotrophic
1010 Marine Magnetotactic Coccus Strain MC-1. *Appl Environ Microbiol* **75**, 4835–4852
1011 (2009).

1012 41. Morillo, V. *et al.* Isolation, cultivation and genomic analysis of magnetosome
1013 biomineralization genes of a new genus of South-seeking magnetotactic cocci within
1014 the Alphaproteobacteria. *Frontiers in Microbiology* **5**, (2014).
1015 42. Koziaeva, V. *et al.* Genome-Based Metabolic Reconstruction of a Novel Uncultivated
1016 Freshwater Magnetotactic coccus “Ca. Magnetaquicoccus inordinatus” UR-1, and
1017 Proposal of a Candidate Family “Ca. Magnetaquicoccaceae”. *Frontiers in*
1018 *Microbiology* **10**, (2019).
1019 43. Abreu, F. *et al.* Cell Adhesion, Multicellular Morphology, and Magnetosome
1020 Distribution in the Multicellular Magnetotactic Prokaryote Candidatus Magnetoglobus
1021 multicellularis. *Microscopy and Microanalysis* **19**, 535–543 (2013).
1022 44. Abreu, F. *et al.* ‘Candidatus Magnetoglobus multicellularis’, a multicellular,
1023 magnetotactic prokaryote from a hypersaline environment. *International Journal of*
1024 *Systematic and Evolutionary Microbiology* **57**, 1318–1322 (2007).
1025 45. Abreu, F. *et al.* Deciphering unusual uncultured magnetotactic multicellular
1026 prokaryotes through genomics. *The ISME Journal* **8**, 1055–1068 (2014).
1027 46. Leão, P. *et al.* Ultrastructure of ellipsoidal magnetotactic multicellular prokaryotes
1028 depicts their complex assemblage and cellular polarity in the context of
1029 magnetotaxis. *Environmental Microbiology* **19**, 2151–2163 (2017).
1030 47. Zhang, R. *et al.* Characterization and phylogenetic identification of a species of
1031 spherical multicellular magnetotactic prokaryotes that produces both magnetite and
1032 greigite crystals. *Research in Microbiology* **165**, 481–489 (2014).
1033 48. Kolinko, S., Richter, M., Glöckner, F.-O., Brachmann, A. & Schüler, D. Single-cell
1034 genomics reveals potential for magnetite and greigite biomineralization in an
1035 uncultivated multicellular magnetotactic prokaryote. *Environmental Microbiology*
1036 *Reports* **6**, 524–531 (2014).
1037 49. Lefèvre, C. T. *et al.* A Cultured Greigite-Producing Magnetotactic Bacterium in a
1038 Novel Group of Sulfate-Reducing Bacteria. *Science* **334**, 1720–1723 (2011).
1039 50. Lefèvre, C. T. *et al.* Comparative genomic analysis of magnetotactic bacteria from
1040 the Deltaproteobacteria provides new insights into magnetite and greigite
1041 magnetosome genes required for magnetotaxis. *Environmental Microbiology* **15**,
1042 2712–2735 (2013).

1043 51. Sakaguchi, T., Burgess, J. G. & Matsunaga, T. Magnetite formation by a sulphate-
1044 reducing bacterium. *Nature* **365**, 47–49 (1993).
1045 52. Sakaguchi, T., Arakaki, A. & Matsunaga, T. Desulfovibrio magneticus sp. nov., a
1046 novel sulfate-reducing bacterium that produces intracellular single-domain-sized
1047 magnetite particles. *International Journal of Systematic and Evolutionary*
1048 *Microbiology* **52**, 215–221 (2002).
1049 53. Nakazawa, H. *et al.* Whole genome sequence of *Desulfovibrio magneticus* strain
1050 RS-1 revealed common gene clusters in magnetotactic bacteria. *Genome Res.* **19**,
1051 1801–1808 (2009).
1052 54. Shimoshige, H. *et al.* Isolation and cultivation of a novel sulfate-reducing
1053 magnetotactic bacterium belonging to the genus Desulfovibrio. *PLoS ONE* **16**,
1054 e0248313 (2021).
1055 55. Lefèvre, C. T., Frankel, R. B., Pósfai, M., Prozorov, T. & Bazylinski, D. A. Isolation of
1056 obligately alkaliphilic magnetotactic bacteria from extremely alkaline environments.
1057 *Environmental Microbiology* **13**, 2342–2350 (2011).
1058 56. Li, J. *et al.* Intracellular silicification by early-branching magnetotactic bacteria. *Sci.*
1059 *Adv.* **8**, eabn6045 (2022).
1060 57. Li, J. *et al.* Crystal growth of bullet-shaped magnetite in magnetotactic bacteria of
1061 the *Nitrospirae* phylum. *J. R. Soc. Interface.* **12**, 20141288 (2015).
1062 58. Lin, W. *et al.* Genomic insights into the uncultured genus 'Candidatus
1063 Magnetobacterium' in the phylum Nitrospirae. *ISME J* **8**, 2463–2477 (2014).
1064 59. Spring, S. *et al.* Dominating Role of an Unusual Magnetotactic Bacterium in the
1065 Microaerobic Zone of a Freshwater Sediment. *Appl Environ Microbiol* **59**, 2397–
1066 2403 (1993).
1067 60. Kolinko, S., Richter, M., Glöckner, F.-O., Brachmann, A. & Schüler, D. Single-cell
1068 genomics of uncultivated deep-branching magnetotactic bacteria reveals a
1069 conserved set of magnetosome genes. *Environmental Microbiology* **18**, 21–37
1070 (2016).
1071 61. Uzun, M. *et al.* Detection of interphylum transfers of the magnetosome gene cluster
1072 in magnetotactic bacteria. *Front. Microbiol.* **13**, 945734 (2022).

62. Zhao, Y. *et al.* Insight into the metabolic potential and ecological function of a novel Magnetotactic Nitrospirota in coral reef habitat. *Front. Microbiol.* **14**, 1182330 (2023).
63. Kolinko, S. *et al.* Single-cell analysis reveals a novel uncultivated magnetotactic bacterium within the candidate division OP3. *Environmental Microbiology* **14**, 1709–1721 (2012).
64. Rahn-Lee, L. *et al.* A Genetic Strategy for Probing the Functional Diversity of Magnetosome Formation. *PLoS Genet* **11**, e1004811 (2015).
65. Grant, C. R., Rahn-lee, L. & Legault, K. N. Genome Editing Method for the Anaerobic Magnetotactic. *Applied and Environmental Microbiology* **84**, 1–12 (2018).